

# Unsupervised Learning of Non-Hermitian Topological Phases

Li-Wei Yu<sup>1</sup> and Dong-Ling Deng<sup>1,2,\*</sup>

<sup>1</sup>Center for Quantum Information, IIIS, Tsinghua University, Beijing 100084, People's Republic of China

<sup>2</sup>Shanghai Qi Zhi Institute, 41th Floor, AI Tower, No. 701 Yunjin Road, Xuhui District, Shanghai 200232, China

(Dated: December 16, 2021)

Non-Hermitian topological phases bear a number of exotic properties, such as the non-Hermitian skin effect and the breakdown of conventional bulk-boundary correspondence. In this paper, we introduce an unsupervised machine learning approach to classify non-Hermitian topological phases based on diffusion maps, which are widely used in manifold learning. We find that the non-Hermitian skin effect will pose a notable obstacle, rendering the straightforward extension of unsupervised learning approaches to topological phases for Hermitian systems ineffective in clustering non-Hermitian topological phases. Through theoretical analysis and numerical simulations of two prototypical models, we show that this difficulty can be circumvented by choosing the “on-site” elements of the projective matrix as the input data. Our results provide a valuable guidance for future studies on learning non-Hermitian topological phases in an unsupervised fashion, both in theory and experiment.

Non-Hermiticity arises naturally in a wide range of scenarios [1–3], such as photonic systems with loss and gain [4–8], open quantum systems [9–12], and quasiparticles with finite lifetimes [13–17]. Recently, the study of non-Hermitian topological phases has attracted tremendous attentions [17–61]. Exciting progresses have been made in both theory [17–51] and experiment [52–61]. One of the prominent phenomena of non-Hermitian systems is the so-called non-Hermitian skin effect (NHSE) [39–42], where the majority of the eigenstates of a non-Hermitian operator are exponentially localized at boundaries. This leads to the breakdown of the conventional bulk-boundary correspondence (a guiding principle for topological phases of Hermitian systems) and calls for the non-Bloch band theory based on the generalized Brillouin zone [32, 41, 42, 50, 51]. The NHSE has been observed in recent experiments [52, 62, 63], and its physical implications and consequences are still under active studies at the current stage [23, 25, 42, 50, 64–71]. Here, we introduce an unsupervised machine learning approach based on diffusion maps to clustering non-Hermitian topological phases, with a focus on these exhibiting NHSE that are drastically distinct from their Hermitian counterparts (see Fig. 1 for a pictorial illustration).

Machine learning techniques [72–74] are exquisitely tailored to identify hidden patterns in complex data and their applications to physics have recently been invoked in various contexts [75–77], ranging from black hole detection [78], gravitational lenses [79] and wave analysis [80, 81], and quantum nonlocality detection [82], to glassy dynamics [83] and material design [84], etc. Within the vein of learning different phases of matter and phase transitions, a number of different approaches have been proposed, with some been demonstrated in recent experiments. In particular, for learning topological phases both supervised [85–92] and unsupervised [93–104] methods have been introduced, despite the fact that topological phases are typically more difficult to learn than conventional symmetry-breaking ones due to their lack of local order parameters [105]. Supervised methods require prior labeling of the data samples, whereas unsupervised learning can detect and classify topological phases from unlabeled raw data, without *a priori* knowledge of the underlying

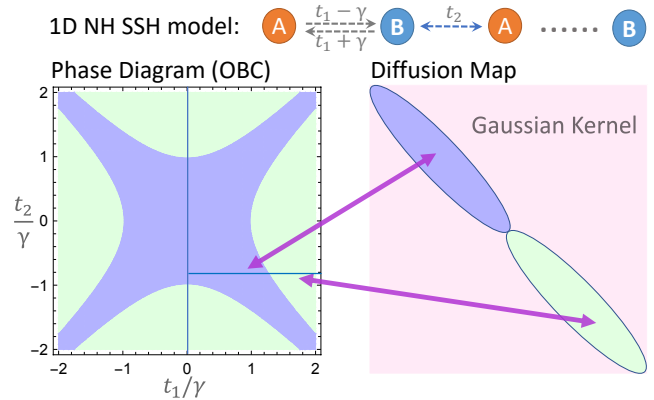


FIG. 1. A schematic illustration of the 1D non-Hermitian Su-Schrieffer-Heeger (NH SSH) model, and the unsupervised learning of its harboring topological phases based on the diffusion map. Theoretically, with open boundary condition (OBC) this model entails two distinct phases with phase diagram shown in the lower-left subfigure. Samples from the same phase correspond to the same diagonal blocks of the Gaussian kernel matrix and the boundary between two blocks indicates the topological phase transition point.

topological mechanism. Therefore, to some extent unsupervised approaches are more powerful and practical in detecting and identifying new topological phases. An intriguing unsupervised approach is based on diffusion maps [106–108], which naturally implements the notion of continuous deformation (homotopy) and thus is particularly suitable for classifying topological objects. Along this line, notable works have demonstrated that diffusion maps are strikingly effective in clustering topological orders in the Ising gauge theory [93], symmetry protected topological phases [94, 95], valence-bond solid [97], and topological phononics [96]. Nevertheless, most of these existing works focus on Hermitian systems and learning of non-Hermitian topological phases, especially for these with NHSE, remains largely unexplored.

In this paper, we use diffusion maps to cluster non-Hermitian topological phases in an unsupervised fashion. Through theoretical analysis, we find that the NHSE gives rise to unwanted singularities that result in vanishing diffusion

probabilities even for data samples from the same topological phase, thus making the direct application of the diffusion map method impotent for classifying non-Hermitian topological phases with skin effect. To overcome this obstacle, we propose to use only the “on-site” elements  $\{P_{iA,iB}|i \in [1, N]\}$  of the projective matrices  $P$ , which are typically used for defining topological indices for non-Hermitian systems, as input data and show, through concrete examples involving one-dimensional (1D) non-Hermitian Su-Schrieffer-Heeger (SSH) and 2D Qi-Wu-Zhang (QWZ) models, that the diffusion map method is indeed capable of classifying non-Hermitian topological phases without supervision, even for these with the NHSE if we use the adjusted input data.

*Theoretical analysis.*—Suppose we are given a set of input data  $\mathbf{D} = \{\mathbf{x}^{(1)}, \mathbf{x}^{(2)}, \dots, \mathbf{x}^{(L)}\}$  coming from different non-Hermitian topological phases. Our goal is to classify these samples topologically, namely, determine the number of different topological phases and for each sample identify which category it belongs to. To measure the local similarity between samples  $\mathbf{x}^{(l)}$  and  $\mathbf{x}^{(l')}$ , we use the Gaussian kernel function with variance controlled by the parameter  $\epsilon$  ( $0 < \epsilon \ll 1$ ):

$$\mathcal{K}_{l,l'} = \exp\left(-\|\mathbf{x}^{(l)} - \mathbf{x}^{(l')}\|_{\mathbb{L}_1}^2 / (2\epsilon N^2)\right), \quad (1)$$

where  $\|\mathbf{x}^{(l)} - \mathbf{x}^{(l')}\|_{\mathbb{L}_1}$  denotes the Taxicab  $\mathbb{L}_1$ -norm distance, i.e.  $\|\mathbf{A}\|_{\mathbb{L}_1} = \sum_i |A_i|$ .  $N$  denotes the number of unit cells of the Hamiltonian. The one-step diffusion probability  $\mathcal{P}_{l,l'}$  from sample  $\mathbf{x}^{(l)}$  to  $\mathbf{x}^{(l')}$  is defined as:  $\mathcal{P}_{l,l'} = \frac{\mathcal{K}_{l,l'}}{\sum_{l'} \mathcal{K}_{l,l'}}$ . After  $2t$  steps, the diffusion distance between  $\mathbf{x}^{(j)}$  and  $\mathbf{x}^{(j')}$  is  $D_t(j, j') = \sum_k \frac{(\mathcal{P}_{j,k}^{2t} - \mathcal{P}_{j',k}^{2t})^2}{\sum_l \mathcal{K}_{k,l}} = \sum_k \lambda_k^{2t} [(\psi_k)_j - (\psi_k)_{j'}]^2$ , where  $\{\psi_k\}$  are the right eigenvectors of  $\mathcal{P}$  and  $\{\lambda_k\}$  denotes their corresponding eigenvalues. From  $D_t$ , it is clear that in the long-time limit  $t \rightarrow \infty$ , only the few components with largest  $|\lambda| \approx 1$  will dominate, and these few components can be used for dimensional reduction and clustering non-Hermitian topological phases.

The success of the diffusion map method relies crucially on the input data samples. For learning topological phases in an unsupervised way, two types of data samples have been considered in previous works [93–97]: bulk Hamiltonian vectors (or equivalently bulk states) in the momentum space and full projective matrices in real space. For Hermitian systems, these two types of data should lead to the same classification due to the bulk-boundary correspondence. However, for non-Hermitian systems the phase transition points might be boundary sensitive and the conventional bulk-boundary correspondence may not hold. As a result, the choice of input data becomes subtle, especially for these topological phases with NHSE. In particular, in the following discussion we will show that the data set of full projective matrices cannot be employed for clustering non-Hermitian topological phases with NHSE via the diffusion map method.

For simplicity and concreteness, we consider spinless non-Hermitian topological models with both periodic and open boundary conditions (abbreviated as PBC and OBC, respec-

tively). To apply the first-order perturbation theory, here we only focus on the lattice models with discrete eigenvalues.

We start with a general two-band model with PBC in the momentum space:  $\hat{H} = \vec{\mathbf{d}} \cdot \vec{\sigma} = d_x \sigma_x + d_y \sigma_y + d_z \sigma_z$ , where  $\sigma_{x,y,z}$  denotes the usual Pauli matrices and  $d_{x,y,z}$  is complex for non-Hermitian systems. As discussed in previous papers [93–95], we may choose the input data sample to be  $\mathbf{x}^{(l)} = \{\hat{\mathbf{d}}^{(l)}(\vec{k})|\vec{k} \in \text{BZ}\}$  with  $\hat{\mathbf{d}} = \frac{\vec{\mathbf{d}}}{\sqrt{d_x^2 + d_y^2 + d_z^2}}$  and BZ denoting the first Brillouin zone. By varying the model parameters  $\vec{t} = (t_1, t_2, \dots)$  contained implicitly in  $\hat{\mathbf{d}}$ , one obtains the input data set  $\{\mathbf{x}^{(l)}\}$ . We now analyze how the diffusion map method can classify these samples into different categories. From the definition of the one-step diffusion probability, it is clear that the dominant terms are these corresponding to the nearest samples labeled by  $(l, l + \delta l)$  [109]. By adjusting the hyper parameter  $\epsilon$ , one can show that the connectivity between  $\mathbf{x}^{(l)}$  and  $\mathbf{x}^{(l + \delta l)}$  depends on the derivability of the unit vector  $\hat{\mathbf{d}}^{(l)} = \vec{\mathbf{d}}^{(l)} / E_+^{(l)}$  on  $\vec{t}$  for all  $k_i \in [-\pi, \pi]$ , where  $E_+^{(l)} = \sqrt{d_x^2 + d_y^2 + d_z^2}$ . The gap closure points  $E_{\pm}^{(l)} = 0$  typically break the derivability. Hence, two samples  $(l, l + \delta l)$  separated by the gap closure point should result in  $\mathcal{K}_{l, l + \delta l} \approx 0$ , i.e. vanishing one-step diffusion probability between them. Combined with the approximation that only the nearest samples dominantly contribute to the diffusion, the gap closure points divide the kernel matrix into blocks, and samples corresponding the same block are connected via diffusion, hence belonging to the same topological phase. Thus for those models with phase transition occurring at the gap closure points, the data samples in the same phase should be clustered into the same category via the diffusion map.

With OBC, things become tricky due to the possible existence of the NHSE. In this case, a straightforward choice for the input data would be the projective matrices defined as  $P = \sum_{\text{Re}[E_m] < 0} |m_R\rangle \langle m_L|$  [43], where  $|m_R\rangle$  and  $\langle m_L|$  are the right and left eigenstates (with the corresponding eigenenergy  $E_m$  and  $E_m^*$  respectively) of the non-Hermitian Hamiltonian in real space. We mention that  $P$  can be used to define the topological invariants for non-Hermitian systems in real space [43]. The  $\mathbb{L}_1$ -norm of a matrix is defined by  $\|P\|_{\mathbb{L}_1} = \sum_{i,j} |P_{ij}|$ . As was mentioned above, the nearest samples dominantly contribute to the diffusion probability with proper hyper parameter  $\epsilon$ . Then the Gaussian kernel can be expressed as  $\mathcal{K}_{l, l + \delta l} = \exp\left(-\frac{\|\delta P\|_{\mathbb{L}_1}^2}{2\epsilon N^2}\right) = \exp\left(-\frac{(\|\nabla_{\vec{t}} P\|_{\mathbb{L}_1} \cdot \delta \vec{t})^2}{2\epsilon N^2}\right)$ .

The singularity of  $\|\nabla_{\vec{t}} P\|_{\mathbb{L}_1}$  is crucial to the kernel values. For convenient illustration, let us take the one-dimensional (1D) non-Hermitian SSH model with OBC (in Fig. 1) as an example, where the fermion annihilation (creation) operators on the A and B sublattices are denoted by  $C_A$  ( $C_A^\dagger$ ) and  $C_B$  ( $C_B^\dagger$ ), respectively;  $t_1$ ,  $t_2$ , and  $\gamma$  are model parameters characterizing the hopping strength. A sketch of the phase diagram is shown in Fig. 1. We consider the parameter region  $t_1 > |\gamma|$ , where the non-Hermitian SSH Hamiltonian  $\hat{H}_o^{1D}$  in orthonormal bases can be transformed into a Her-

mitian matrix  $\hat{H}_o^{1D}$  in non-orthonormal bases [41]:  $\bar{H}_o^{1D} = \Gamma^{-1} \hat{H}_o^{1D} \Gamma$  with  $\Gamma = \text{diag}(1, r, r, r^2, r^2, \dots, r^{N-1}, r^N)$ , and  $r = \sqrt{|(t_1 - \gamma)/(t_1 + \gamma)|}$ . Then  $\partial_{t_1} P$  reduces to [110]:

$$\partial_{t_1} P = \sum_{\substack{\text{Re}[E_m] < 0 \\ n \neq m}} \frac{\langle n | \Gamma \partial_{t_1} \hat{H} \Gamma^{-1} | m \rangle \Gamma^{-1} | n \rangle \langle m | \Gamma + (n \leftrightarrow m)}{E_m - E_n}.$$

Direct calculations show that all terms  $\langle n | \Gamma \partial_{t_1} \hat{H}_o^{1D} \Gamma^{-1} | m \rangle / N$  are finite [110]. Suppose the system is initially in the topologically trivial phase, then when the system approaches the phase transition point  $|t_1| = \sqrt{t_2^2 + \gamma^2}$ , the two levels  $E_{\pm 1}$  approach zero and become the zero modes, which will be eliminated in the  $P$ -matrix after passing through the transition point. The only singularity ( $|t_1| \neq |\gamma|$ ) of  $1/(E_m - E_n)$  occurs at the gap closing point, where the two nearest levels  $|E_{-1} - E_1| \rightarrow 0$ . So far, everything looks similar to the Hermitian SSH model. However, the term  $\Gamma^{-1} | n \rangle \langle m | \Gamma$ , which basically gives rise to the NHSE, involves matrix elements with values  $r^{\pm(i-j+1)}$  that are singular when  $|i-j| \rightarrow \infty$ . This singularity is boundary condition sensitive and unique to non-Hermitian systems. It persists for a wide range of parameter space, independent of the phase transitions. As a consequence, it will render the diffusion map method invalid and should be removed from the input data. To address this problem, we propose to use the ‘‘on-site’’ part of the  $P$ -matrix elements as the raw input data:  $\{P_{iA, iB} | i \in [1, N]\}$ , where  $r^{\pm(i-j+1)}$  factors cancel out and no singularity shows up. Such ‘‘on-site’’ extraction should be suitable to those non-Hermitian models where the NHSE exhibits an exponential function of lattice site. With this adjusted  $P$ -matrix as the input data, the kernel values  $\mathcal{K}_{l, l+\delta l} \approx 1$  for all the data samples from the same phase, but two samples  $\{l, l+\delta l\}$  crossing the phase transition point have no connectivity  $\mathcal{K}_{l, l+\delta l} \approx 0$ . This restores the capability of the diffusion map method in classifying non-Hermitian topological phases with NHSE in the unsupervised fashion.

The above discussion explains in theory why and when the diffusion map method can be applied to classify non-Hermitian topological phases, and how to overcome the obstacles due to the NHSE. To illustrate how this method works in practice, in the following we apply it to a couple of concrete examples, including the cases with and without the NHSE.

*Unsupervised learning without NHSE.*—The first example we consider is the non-Hermitian SSH model with PBC. In the momentum space, this model reads  $H_p(k) = \vec{d} \cdot \vec{\sigma} = (t_1 + t_2 \cos k) \sigma_x + (t_2 \sin k + i\gamma) \sigma_y$ . The input data set can be chosen as  $\{\mathbf{x}^{(l)} | \mathbf{x}^{(l)} = \hat{\mathbf{d}}(k_i), |k_i = \frac{2i-N-2}{N} \pi, i \in [1, N]\}$  with varying  $t_1$ , while fixing  $t_2$  and  $\gamma$ . Our numerical results are shown in Fig. 2 (a-c). From Fig. 2 (a), the kernel matrix  $\mathcal{K}$  is separated into three blocks, which correspond to the three largest eigenvalues  $\lambda_{0,1,2} \approx 1$  of the one-step diffusion matrix  $\mathcal{P}$ , as shown in Fig. 2 (b). As a result, the input samples are classified into three different topological phases. This is also clearly indicated in Fig. 2 (c), where we show the scatter diagram of eigenvectors  $\{\psi_1, \psi_2\}$  corresponding to  $\lambda_{1,2}$ .

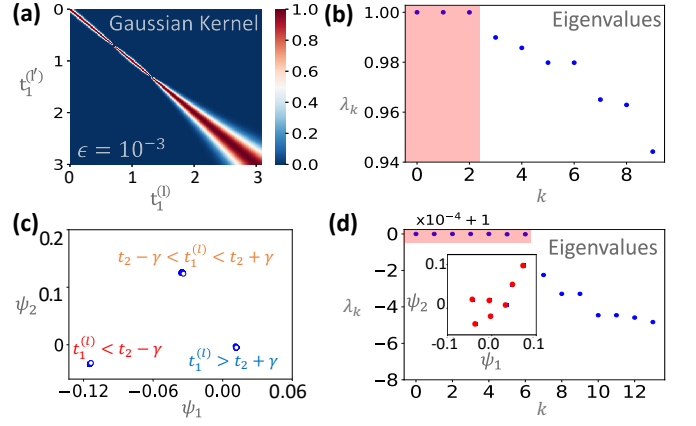


FIG. 2. Numerical results of unsupervised learning without NHSE for the 1D non-Hermitian SSH [subfigures (a-c)] and 2D QWZ model [subfigure (d)]. (a) Heatmap for Gaussian kernel value distribution between samples with varying  $t_1$ . (b) Eigenvalues of the one-step diffusion matrix  $\mathcal{P}$ . (c) Scatter diagram of eigenvectors  $\{\psi_1, \psi_2\}$  with the corresponding eigenvalues  $\lambda_{1,2} \approx 1$ , where the samples are clustered into three topological phases. (d) For the QWZ model, the input samples are classified into seven categories [110].

In addition, the phase boundaries can also be obtained from Fig. 2 (a), which match exactly with the theoretical one [110].

Another example we consider is the 2D non-Hermitian QWZ model with PBC:  $\hat{H}_p^{2D}(\mathbf{k}) = (v_x \sin k_x + i\gamma_x) \sigma_x + (v_y \sin k_y + i\gamma_y) \sigma_y + (M - 0.5 \cos k_x - 0.5 \cos k_y) \sigma_z$ . The phase boundaries occur at  $M_{\pm}^{(\nu)} = (2-\nu) \pm \sqrt{\gamma_x^2 + \gamma_y^2}$ ,  $\nu = 1, 2, 3$ . The Hamiltonian in the region  $M \in (-\infty, M_+^{(3)}) \cup (M_+^{(3)}, M_-^{(2)}) \cup (M_-^{(2)}, M_+^{(2)}) \cup (M_+^{(2)}, M_-^{(1)}) \cup (M_-^{(1)}, M_+^{(1)}) \cup (M_+^{(1)}, +\infty)$  is gapped and the topological Chern number is well-defined. However, in regions  $M \in (M_-^{(\nu)}, M_+^{(\nu)})$  the Hamiltonian is gapless and the topological indices are not well-defined. These gapless regions lead to singularities and hence no diffusion probability among samples from such regions. Nevertheless, one can still utilize the diffusion map method to locate the phase boundaries  $M_{\pm}^{(1,2,3)}$  based on the ‘‘effective’’ kernel matrix, which is the average of a set of kernel matrices with different lattice sizes (different discrete  $\vec{k}$  configurations) as the input data. By such a construction, the diffusion map method still works even with input samples in gapless regions. We choose the bulk Hamiltonian as the input samples by varying the parameter  $M$  and our numerical results are shown in Fig. 2 (d). From this figure, the samples are classified into seven categories. In addition, careful examinations of the heatmap for the kernel matrix yield that the phase boundaries identified by the diffusion map method coincide with the theoretical ones [110].

*Unsupervised learning with NHSE.*—The above numerical results show clearly that the diffusion map method is indeed capable of classifying non-Hermitian topological phases without NHSE. Yet, as discussed in the beginning the presence of the NHSE may handicap the performance of this approach. A possible way out of this is to choose different input data. Now, we turn to this case and examine the applicability of the dif-

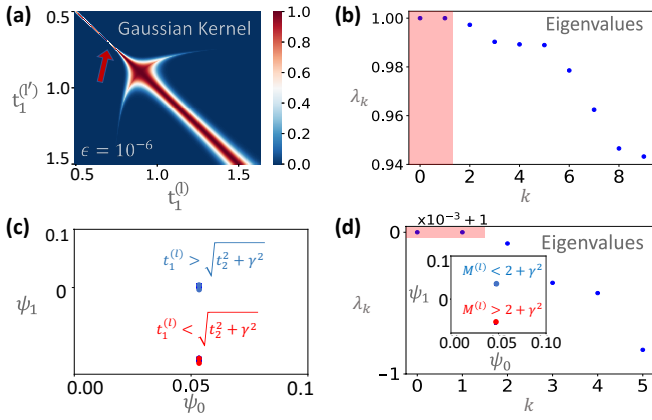


FIG. 3. Numerical results of unsupervised learning with NHSE. (a-c) show respectively the heatmap of the Gaussian kernel, the eigenvalues of the one-step diffusion matrix, and the scatter diagram of eigenvectors for the non-Hermitian SSH model. The red arrow in (a) indicates the phase transition point  $t_1 \approx 0.6993$ . The input data samples are clustered into two (rather than three) topological categories, in sharp contrast to the case of learning without NHSE shown in Fig. 2. (d) The eigenvalues of the one-step diffusion matrix for the non-Hermitian QWZ model, with the inset showing the scatter diagram of eigenvectors corresponding to the largest two eigenvalues. The input samples are classified into two (rather than seven) categories [110].

fusion map method for clustering non-Hermitian topological phases with NHSE. We still focus on the non-Hermitian SSH and QWZ models, but with OBCs this time.

We start with the 1D non-Hermitian SSH model [41]. With OBC, the phase boundaries are theoretically predicted to be  $t_1 = \pm\sqrt{t_2^2 + \gamma^2}$ . Topological non-trivial phase with ground state degeneracy occurs in the interval  $|t_1| < \sqrt{t_2^2 + \gamma^2}$ . We numerically diagonalize the real space Hamiltonian  $\hat{H}_o^{1D}$  for given system sizes and parameters, and choose partial elements of the projective matrices  $\{P_{iA,iB}^{(l)} | i \in [1, N]\}$  as the raw input data  $\{\mathbf{x}^{(l)}\}$ . Our numerical results are shown in Fig. S2 (a-c). From this figure, the input samples are classified into two categories and the learnt phase transition point occurs at  $t_1 \approx 0.6993$ , which is consistent with theoretically predicted values of  $t_1 = \sqrt{t_2^2 + \gamma^2} \approx 0.7211$  [110]. The small discrepancy is mainly due to the fact that only partial information of the projective matrices are used and the finite size effect in our numerical simulations (see [110] for details).

For the 2D non-Hermitian QWZ model with OBC, it has been shown from both analytical and numerical aspects that one topological phase boundary occurs approximately at  $M = M_0 = t_x + t_y + \frac{t_x \gamma_x^2}{2v_x^2} + \frac{t_y \gamma_y^2}{2v_y^2}$  for small  $\frac{\gamma_{x(y)}}{v_{x(y)}}$  [42]. When  $M < M_0$ , the corresponding Chern number in generalized Brillouin zone for the valence band ( $\text{Re}(E) < 0$ ) is  $C = 1$ . Whereas for  $M > M_0$ , the Chern number is  $C = 0$ . With partial elements of the projective matrices as input data, the diffusion map method works as well and our numerical results are shown in Fig. S2 (d). It is clear from this figure that the input samples are classified into two distinct categories and the

learnt phase boundary occurs at  $M \approx 2.1731$ , which matches the theoretical value  $M = 2.2$  with a desirable accuracy [110].

We mention that non-Hermitian systems are extremely sensitive to boundary conditions. A change of boundary conditions could alter drastically both the eigenspectra and eigenstates [111]. This is in sharp contrast to the case of Hermitian systems. From the unsupervised learning results shown above, it is also clear that different boundary conditions lead to completely different clustering results of the input samples. For instance, with PBC the data samples of the QWZ model are clustered into seven groups via the diffusion map method, whereas with OBC one obtains only two categories. Owing to the NHSE, the relevant features of input data could be dramatically suppressed and consequently are harder to extract. Here we note that the obstacle induced by the NHSE may also exist in other machine learning approaches, e.g., the CNN-based ones [91], and the solution we provide here should carry over to these algorithms as well [110]. We also remark that finding the appropriate topological invariants based on the projective matrix is a highly non-trivial task. In fact, a number of works have been reported recently in the literature to deal with this problem [30, 39, 43, 112]. Although the diffusion map approach still requires full diagonalization of Hamiltonians in real space, it does not rely on any *a priori* information about the underlying topological invariants. As a result, this approach is also applicable to non-Hermitian systems whose characteristic topological invariants have not yet been discovered. In addition, the requirement of the costly diagonalization might be circumvented by replacing the projective matrix with observables (e.g., correlation functions) that can be measured in experiment. We leave this interesting and important problem for future studies.

*Discussion and conclusion.*—Symmetries play a crucial role in the study of topological phases and, analogous to the Hermitian case [113], a periodic table for non-Hermitian Hamiltonians has also been established from the  $K$  theory perspective recently [29]. Yet, incorporating symmetry constraints into unsupervised learning approaches to topological phases is highly nontrivial [94]. In the future, it would be interesting and desirable to extend our results to symmetry protected or enriched non-Hermitian topological phases, especially those predicted in the periodic table. In addition, non-Hermitian topological phases for interacting systems remain elusive and we expect that unsupervised learning will provide valuable wisdom in studying such phases as well.

In summary, we have introduced an unsupervised machine learning approach to classify non-Hermitian topological phases based on diffusion maps. We show that the NHSE can result in a critical handicap for the straightforward extension of the unsupervised method of learning Hermitian topological phases to the non-Hermitian case. Through theoretical analysis and numerical simulations, we have demonstrated that this obstacle can be avoided by appropriately choosing the input data, such as the “on-site” elements of the projective matrices. Our results reveal a new consequence of the NHSE and would benefit future studies across non-Hermitian topological

phases and machine learning.

We acknowledge Mathias S. Scheurer for sharing his previous programming code on diffusion map with us. This work was supported by the start-up fund from Tsinghua University (Grant No. 53330300320) and the National Natural Science Foundation of China (Grant No. 11905108). DLD also would like to acknowledge additional support from the Shanghai Qi Zhi Institute.

---

\* [dldeng@tsinghua.edu.cn](mailto:dldeng@tsinghua.edu.cn)

- [1] N. Moiseyev, *Non-Hermitian quantum mechanics* (Cambridge University Press, 2011).
- [2] V. V. Konotop, J. Yang, and D. A. Zezyulin, Nonlinear waves in  $\mathcal{PT}$ -symmetric systems, *Rev. Mod. Phys.* **88**, 035002 (2016).
- [3] Y. Ashida, Z. Gong, and M. Ueda, Non-Hermitian Physics, [arXiv:2006.01837](https://arxiv.org/abs/2006.01837) (2020).
- [4] L. Feng, R. El-Ganainy, and L. Ge, Non-Hermitian photonics based on parity–time symmetry, *Nat. Photon.* **11**, 752 (2017).
- [5] R. El-Ganainy, K. G. Makris, M. Khajavikhan, Z. H. Musslimani, S. Rotter, and D. N. Christodoulides, Non-Hermitian physics and PT symmetry, *Nat. Phys.* **14**, 11 (2018).
- [6] M.-A. Miri and A. Alu, Exceptional points in optics and photonics, *Science* **363**, eaar7709 (2019).
- [7] Ş. Özdemir, S. Rotter, F. Nori, and L. Yang, Parity–time symmetry and exceptional points in photonics, *Nat. Mater.* **18**, 783 (2019).
- [8] T. Ozawa, H. M. Price, A. Amo, N. Goldman, M. Hafezi, L. Lu, M. C. Rechtsman, D. Schuster, J. Simon, O. Zilberberg, and I. Carusotto, Topological photonics, *Rev. Mod. Phys.* **91**, 015006 (2019).
- [9] I. Rotter, A non-Hermitian Hamilton operator and the physics of open quantum systems, *J. Phys. A: Math. Theor.* **42**, 153001 (2009).
- [10] B. Zhen, C. W. Hsu, Y. Igarashi, L. Lu, I. Kaminer, A. Pick, S.-L. Chua, J. D. Joannopoulos, and M. Soljačić, Spawning rings of exceptional points out of Dirac cones, *Nature* **525**, 354 (2015).
- [11] S. Diehl, E. Rico, M. A. Baranov, and P. Zoller, Topology by dissipation in atomic quantum wires, *Nat. Phys.* **7**, 971 (2011).
- [12] F. Verstraete, M. M. Wolf, and J. I. Cirac, Quantum computation and quantum-state engineering driven by dissipation, *Nat. Phys.* **5**, 633 (2009).
- [13] V. Kozii and L. Fu, Non-Hermitian topological theory of finite-lifetime quasiparticles: prediction of bulk Fermi arc due to exceptional point, [arXiv:1708.05841](https://arxiv.org/abs/1708.05841) (2017).
- [14] A. A. Zyuzin and A. Y. Zyuzin, Flat band in disorder-driven non-Hermitian Weyl semimetals, *Phys. Rev. B* **97**, 041203(R) (2018).
- [15] H. Shen and L. Fu, Quantum Oscillation from In-Gap States and a Non-Hermitian Landau Level Problem, *Phys. Rev. Lett.* **121**, 026403 (2018).
- [16] H. Zhou, C. Peng, Y. Yoon, C. W. Hsu, K. A. Nelson, L. Fu, J. D. Joannopoulos, M. Soljačić, and B. Zhen, Observation of bulk Fermi arc and polarization half charge from paired exceptional points, *Science* **359**, 1009 (2018).
- [17] T. Yoshida, R. Peters, and N. Kawakami, Non-Hermitian perspective of the band structure in heavy-fermion systems, *Phys. Rev. B* **98**, 035141 (2018).
- [18] Y. Xu, S.-T. Wang, and L.-M. Duan, Weyl Exceptional Rings in a Three-Dimensional Dissipative Cold Atomic Gas, *Phys. Rev. Lett.* **118**, 045701 (2017).
- [19] F. K. Kunst, E. Edvardsson, J. C. Budich, and E. J. Bergholtz, Biorthogonal Bulk-Boundary Correspondence in Non-Hermitian Systems, *Phys. Rev. Lett.* **121**, 026808 (2018).
- [20] Y. Chen and H. Zhai, Hall conductance of a non-Hermitian Chern insulator, *Phys. Rev. B* **98**, 245130 (2018).
- [21] J. Y. Lee, J. Ahn, H. Zhou, and A. Vishwanath, Topological Correspondence between Hermitian and Non-Hermitian Systems: Anomalous Dynamics, *Phys. Rev. Lett.* **123**, 206404 (2019).
- [22] T. E. Lee, Anomalous Edge State in a Non-Hermitian Lattice, *Phys. Rev. Lett.* **116**, 133903 (2016).
- [23] L. Jin and Z. Song, Bulk-boundary correspondence in a non-Hermitian system in one dimension with chiral inversion symmetry, *Phys. Rev. B* **99**, 081103(R) (2019).
- [24] D. Carvalho, N. A. García-Martínez, J. L. Lado, and J. Fernández-Rossier, Real-space mapping of topological invariants using artificial neural networks, *Phys. Rev. B* **97**, 115453 (2018).
- [25] C. H. Lee and R. Thomale, Anatomy of skin modes and topology in non-Hermitian systems, *Phys. Rev. B* **99**, 201103(R) (2019).
- [26] D. Leykam, K. Y. Bliokh, C. Huang, Y. D. Chong, and F. Nori, Edge Modes, Degeneracies, and Topological Numbers in Non-Hermitian Systems, *Phys. Rev. Lett.* **118**, 040401 (2017).
- [27] C. Yin, H. Jiang, L. Li, R. Lü, and S. Chen, Geometrical meaning of winding number and its characterization of topological phases in one-dimensional chiral non-Hermitian systems, *Phys. Rev. A* **97**, 052115 (2018).
- [28] K. Kawabata, S. Higashikawa, Z. Gong, Y. Ashida, and M. Ueda, Topological unification of time-reversal and particle-hole symmetries in non-Hermitian physics, *Nat. Commun.* **10**, 1 (2019).
- [29] Z. Gong, Y. Ashida, K. Kawabata, K. Takasan, S. Higashikawa, and M. Ueda, Topological Phases of Non-Hermitian Systems, *Phys. Rev. X* **8**, 031079 (2018).
- [30] K. Kawabata, K. Shiozaki, M. Ueda, and M. Sato, Symmetry and Topology in Non-Hermitian Physics, *Phys. Rev. X* **9**, 041015 (2019).
- [31] H. Shen, B. Zhen, and L. Fu, Topological Band Theory for Non-Hermitian Hamiltonians, *Phys. Rev. Lett.* **120**, 146402 (2018).
- [32] K. Yokomizo and S. Murakami, Non-Bloch Band Theory of Non-Hermitian Systems, *Phys. Rev. Lett.* **123**, 066404 (2019).
- [33] Z.-Y. Ge, Y.-R. Zhang, T. Liu, S.-W. Li, H. Fan, and F. Nori, Topological band theory for non-Hermitian systems from the Dirac equation, *Phys. Rev. B* **100**, 054105 (2019).
- [34] R. A. Molina and J. González, Surface and 3D Quantum Hall Effects from Engineering of Exceptional Points in Nodal-Line Semimetals, *Phys. Rev. Lett.* **120**, 146601 (2018).
- [35] H. Xue, Q. Wang, B. Zhang, and Y. D. Chong, Non-Hermitian Dirac Cones, *Phys. Rev. Lett.* **124**, 236403 (2020).
- [36] J. C. Budich, J. Carlström, F. K. Kunst, and E. J. Bergholtz, Symmetry-protected nodal phases in non-Hermitian systems, *Phys. Rev. B* **99**, 041406(R) (2019).
- [37] T. Yoshida, R. Peters, N. Kawakami, and Y. Hatsugai, Symmetry-protected exceptional rings in two-dimensional correlated systems with chiral symmetry, *Phys. Rev. B* **99**, 121101(R) (2019).
- [38] Z. Yang and J. Hu, Non-Hermitian Hopf-link exceptional line semimetals, *Phys. Rev. B* **99**, 081102(R) (2019).
- [39] N. Okuma, K. Kawabata, K. Shiozaki, and M. Sato, Topolog-

- ical Origin of Non-Hermitian Skin Effects, *Phys. Rev. Lett.* **124**, 086801 (2020).
- [40] L. Li, C. H. Lee, S. Mu, and J. Gong, Critical non-Hermitian Skin Effect, [arXiv:2003.03039](https://arxiv.org/abs/2003.03039) (2020).
- [41] S. Yao and Z. Wang, Edge States and Topological Invariants of Non-Hermitian Systems, *Phys. Rev. Lett.* **121**, 086803 (2018).
- [42] S. Yao, F. Song, and Z. Wang, Non-Hermitian Chern Bands, *Phys. Rev. Lett.* **121**, 136802 (2018).
- [43] F. Song, S. Yao, and Z. Wang, Non-Hermitian Topological Invariants in Real Space, *Phys. Rev. Lett.* **123**, 246801 (2019).
- [44] Z. Yang, C.-K. Chiu, C. Fang, and J. Hu, Jones Polynomial and Knot Transitions in Hermitian and non-Hermitian Topological Semimetals, *Phys. Rev. Lett.* **124**, 186402 (2020).
- [45] T. Bessho and M. Sato, Topological Duality in Floquet and Non-Hermitian Dynamical Anomalies: Extended Nielsen-Ninomiya Theorem and Chiral Magnetic Effect, [arXiv:2006.04204](https://arxiv.org/abs/2006.04204) (2020).
- [46] L. Zhou, Non-Hermitian Floquet phases with even-integer topological invariants in a periodically quenched two-leg ladder, [arXiv:2006.08897](https://arxiv.org/abs/2006.08897) (2020).
- [47] B. Höckendorf, A. Alvermann, and H. Fehske, Topological origin of quantized transport in non-Hermitian Floquet chains, *Phys. Rev. Research* **2**, 023235 (2020).
- [48] C. C. Wojcik, X.-Q. Sun, T. c. v. Bzdušek, and S. Fan, Homotopy characterization of non-Hermitian Hamiltonians, *Phys. Rev. B* **101**, 205417 (2020).
- [49] Z. Li and R. S. Mong, Homotopical classification of non-Hermitian band structures, [arXiv:1911.02697](https://arxiv.org/abs/1911.02697) (2019).
- [50] T. Liu, Y.-R. Zhang, Q. Ai, Z. Gong, K. Kawabata, M. Ueda, and F. Nori, Second-Order Topological Phases in Non-Hermitian Systems, *Phys. Rev. Lett.* **122**, 076801 (2019).
- [51] T.-S. Deng and W. Yi, Non-Bloch topological invariants in a non-Hermitian domain wall system, *Phys. Rev. B* **100**, 035102 (2019).
- [52] L. Xiao, T. Deng, K. Wang, G. Zhu, Z. Wang, W. Yi, and P. Xue, Non-Hermitian bulk–boundary correspondence in quantum dynamics, *Nat. Phys.* **16**, 761 (2020).
- [53] J. M. Zeuner, M. C. Rechtsman, Y. Plotnik, Y. Lumer, S. Nolte, M. S. Rudner, M. Segev, and A. Szameit, Observation of a Topological Transition in the Bulk of a Non-Hermitian System, *Phys. Rev. Lett.* **115**, 040402 (2015).
- [54] C. Poli, M. Bellec, U. Kuhl, F. Mortessagne, and H. Schemm, Selective enhancement of topologically induced interface states in a dielectric resonator chain, *Nat. Commun.* **6**, 6710 (2015).
- [55] S. Weimann, M. Kremer, Y. Plotnik, Y. Lumer, S. Nolte, K. G. Makris, M. Segev, M. C. Rechtsman, and A. Szameit, Topologically protected bound states in photonic parity–time-symmetric crystals, *Nat. Mater.* **16**, 433 (2017).
- [56] W. Chen, Ş. K. Özdemir, G. Zhao, J. Wiersig, and L. Yang, Exceptional points enhance sensing in an optical microcavity, *Nature* **548**, 192 (2017).
- [57] H. Zhou, C. Peng, Y. Yoon, C. W. Hsu, K. A. Nelson, L. Fu, J. D. Joannopoulos, M. Soljačić, and B. Zhen, Observation of bulk Fermi arc and polarization half charge from paired exceptional points, *Science* **359**, 1009 (2018).
- [58] X.-X. Zhang and M. Franz, Non-Hermitian Exceptional Landau Quantization in Electric Circuits, *Phys. Rev. Lett.* **124**, 046401 (2020).
- [59] A. Cerjan, S. Huang, M. Wang, K. P. Chen, Y. Chong, and M. C. Rechtsman, Experimental realization of a Weyl exceptional ring, *Nat. Photon.* **13**, 623 (2019).
- [60] M. A. Bandres, S. Wittek, G. Harari, M. Parto, J. Ren, M. Segev, D. N. Christodoulides, and M. Khajavikhan, Topological insulator laser: Experiments, *Science* **359**, eaar4005 (2018).
- [61] L. Li, C. H. Lee, and J. Gong, Topological Switch for Non-Hermitian Skin Effect in Cold-Atom Systems with Loss, *Phys. Rev. Lett.* **124**, 250402 (2020).
- [62] T. Helbig, T. Hofmann, S. Imhof, M. Abdelghany, T. Kiessling, L. Molenkamp, C. Lee, A. Szameit, M. Greiter, and R. Thomale, Generalized bulk–boundary correspondence in non-Hermitian topoelectrical circuits, *Nat. Phys.* **16**, 747 (2020).
- [63] A. Ghatak, M. Brandenbourger, J. van Wezel, and C. Coulais, Observation of non-Hermitian topology and its bulk–edge correspondence, [arXiv:1907.11619](https://arxiv.org/abs/1907.11619) (2019).
- [64] H.-G. Zirnstein, G. Refael, and B. Rosenow, Bulk–boundary correspondence for non-Hermitian Hamiltonians via Green functions, [arXiv:1901.11241](https://arxiv.org/abs/1901.11241) (2019).
- [65] H. Wang, J. Ruan, and H. Zhang, Non-Hermitian nodal-line semimetals with an anomalous bulk–boundary correspondence, *Phys. Rev. B* **99**, 075130 (2019).
- [66] H. Jiang, L.-J. Lang, C. Yang, S.-L. Zhu, and S. Chen, Interplay of non-Hermitian skin effects and Anderson localization in nonreciprocal quasiperiodic lattices, *Phys. Rev. B* **100**, 054301 (2019).
- [67] C. H. Lee, L. Li, and J. Gong, Hybrid higher-order skin-topological modes in nonreciprocal systems, *Phys. Rev. Lett.* **123**, 016805 (2019).
- [68] E. Edvardsson, F. K. Kunst, and E. J. Bergholtz, Non-Hermitian extensions of higher-order topological phases and their biorthogonal bulk–boundary correspondence, *Phys. Rev. B* **99**, 081302(R) (2019).
- [69] D. S. Borgnia, A. J. Kruchkov, and R.-J. Slager, Non-Hermitian Boundary Modes and Topology, *Phys. Rev. Lett.* **124**, 056802 (2020).
- [70] M. Ezawa, Non-Hermitian boundary and interface states in nonreciprocal higher-order topological metals and electrical circuits, *Phys. Rev. B* **99**, 121411(R) (2019).
- [71] X. Yang, Y. Cao, and Y. Zhai, Non-hermitian weyl semimetals: Non-hermitian skin effect and non-bloch bulk–boundary correspondence, [arXiv:1904.02492](https://arxiv.org/abs/1904.02492) (2019).
- [72] I. Goodfellow, Y. Bengio, and A. Courville, *Deep learning* (MIT press, 2016).
- [73] M. Jordan and T. Mitchell, Machine learning: Trends, perspectives, and prospects, *Science* **349**, 255 (2015).
- [74] Y. LeCun, Y. Bengio, and G. Hinton, Deep learning, *Nature* **521**, 436 (2015).
- [75] V. Dunjko and H. J. Briegel, Machine learning & artificial intelligence in the quantum domain: a review of recent progress, *Rep. Prog. Phys.* **81**, 074001 (2018).
- [76] S. D. Sarma, D.-L. Deng, and L.-M. Duan, Machine learning meets quantum physics, *Physics Today* **72**, 48 (2019).
- [77] G. Carleo, I. Cirac, K. Cranmer, L. Daudet, M. Schuld, N. Tishby, L. Vogt-Maranto, and L. Zdeborová, Machine learning and the physical sciences, *Rev. Mod. Phys.* **91**, 045002 (2019).
- [78] M. Pasquato, Detecting intermediate mass black holes in globular clusters with machine learning, [arXiv:1606.08548](https://arxiv.org/abs/1606.08548) (2016).
- [79] Y. D. Hezaveh, L. Perreault Levasseur, and P. J. Marshall, Fast automated analysis of strong gravitational lenses with convolutional neural networks, *Nature* **548**, 555 (2017).
- [80] R. Biswas, L. Blackburn, J. Cao, R. Essick, K. A. Hodge, E. Katsavounidis, K. Kim, Y.-M. Kim, E.-O. Le Bigot, C.-H. Lee, J. J. Oh, S. H. Oh, E. J. Son, Y. Tao, R. Vaulin, and X. Wang, Application of machine learning algorithms to the

- study of noise artifacts in gravitational-wave data, *Phys. Rev. D* **88**, 062003 (2013).
- [81] B. P. Abbott *et al.* (LIGO Scientific Collaboration and Virgo Collaboration), Observation of gravitational waves from a binary black hole merger, *Phys. Rev. Lett.* **116**, 061102 (2016).
- [82] D.-L. Deng, Machine Learning Detection of Bell Nonlocality in Quantum Many-Body Systems, *Phys. Rev. Lett.* **120**, 240402 (2018).
- [83] S. S. Schoenholz, E. D. Cubuk, D. M. Sussman, E. Kaxiras, and A. J. Liu, A structural approach to relaxation in glassy liquids, *Nat. Phys.* **12**, 469 (2016).
- [84] S. V. Kalinin, B. G. Sumpter, and R. K. Archibald, Big-deep-smart data in imaging for guiding materials design, *Nat. Mater.* **14**, 973 (2015).
- [85] Y. Zhang and E.-A. Kim, Quantum Loop Topography for Machine Learning, *Phys. Rev. Lett.* **118**, 216401 (2017).
- [86] Y. Zhang, R. G. Melko, and E.-A. Kim, Machine learning  $\mathbb{Z}_2$  quantum spin liquids with quasiparticle statistics, *Phys. Rev. B* **96**, 245119 (2017).
- [87] N. Yoshioka, Y. Akagi, and H. Katsura, Learning disordered topological phases by statistical recovery of symmetry, *Phys. Rev. B* **97**, 205110 (2018).
- [88] P. Zhang, H. Shen, and H. Zhai, Machine Learning Topological Invariants with Neural Networks, *Phys. Rev. Lett.* **120**, 066401 (2018).
- [89] N. L. Holanda and M. A. R. Griffith, Machine learning topological phases in real space, *Phys. Rev. B* **102**, 054107 (2020).
- [90] B. Narayan and A. Narayan, Machine learning non-Hermitian topological phases, *Phys. Rev. B* **103**, 035413 (2021).
- [91] L.-F. Zhang, L.-Z. Tang, Z.-H. Huang, G.-Q. Zhang, W. Huang, and D.-W. Zhang, Machine learning topological invariants of non-Hermitian systems, *Phys. Rev. A* **103**, 012419 (2021).
- [92] W. Lian, S.-T. Wang, S. Lu, Y. Huang, F. Wang, X. Yuan, W. Zhang, X. Ouyang, X. Wang, X. Huang, L. He, X. Chang, D.-L. Deng, and L. Duan, Machine Learning Topological Phases with a Solid-State Quantum Simulator, *Phys. Rev. Lett.* **122**, 210503 (2019).
- [93] J. F. Rodriguez-Nieva and M. S. Scheurer, Identifying topological order through unsupervised machine learning, *Nat. Phys.* **15**, 790 (2019).
- [94] M. S. Scheurer and R.-J. Slager, Unsupervised Machine Learning and Band Topology, *Phys. Rev. Lett.* **124**, 226401 (2020).
- [95] Y. Che, C. Gneiting, T. Liu, and F. Nori, Topological quantum phase transitions retrieved through unsupervised machine learning, *Phys. Rev. B* **102**, 134213 (2020).
- [96] Y. Long, J. Ren, and H. Chen, Unsupervised Manifold Clustering of Topological Phononics, *Phys. Rev. Lett.* **124**, 185501 (2020).
- [97] A. Lidiak and Z. Gong, Unsupervised machine learning of quantum phase transitions using diffusion maps, *Phys. Rev. Lett.* **125**, 225701 (2020).
- [98] K. Fukushima, S. S. Funai, and H. Iida, Featuring the topology with the unsupervised machine learning, *arXiv preprint arXiv:1908.00281* (2019).
- [99] F. Schäfer and N. Lörch, Vector field divergence of predictive model output as indication of phase transitions, *Phys. Rev. E* **99**, 062107 (2019).
- [100] O. Balabanov and M. Granath, Unsupervised learning using topological data augmentation, *Phys. Rev. Research* **2**, 013354 (2020).
- [101] C. Alexandrou, A. Athenodorou, C. Chrysostomou, and S. Paul, The critical temperature of the 2d-ising model through deep learning autoencoders, *Eur. Phys. J. B* **93**, 1 (2020).
- [102] E. Greplova, A. Valenti, G. Boschung, F. Schäfer, N. Lörch, and S. D. Huber, Unsupervised identification of topological phase transitions using predictive models, *New Journal of Physics* **22**, 045003 (2020).
- [103] J. Arnold, F. Schäfer, M. Žonda, and A. U. Lode, Interpretable and unsupervised phase classification, *arXiv preprint arXiv:2010.04730* (2020).
- [104] K. Kottmann, P. Huembeli, M. Lewenstein, and A. Acín, Unsupervised phase discovery with deep anomaly detection, *Phys. Rev. Lett.* **125**, 170603 (2020).
- [105] M. J. S. Beach, A. Golubeva, and R. G. Melko, Machine learning vortices at the Kosterlitz-Thouless transition, *Phys. Rev. B* **97**, 045207 (2018).
- [106] R. R. Coifman, S. Lafon, A. B. Lee, M. Maggioni, B. Nadler, F. Warner, and S. W. Zucker, Geometric diffusions as a tool for harmonic analysis and structure definition of data: Diffusion maps, *Proc. Natl. Acad. Sci. USA* **102**, 7426 (2005).
- [107] R. R. Coifman, S. Lafon, A. B. Lee, M. Maggioni, B. Nadler, F. Warner, and S. W. Zucker, Geometric diffusions as a tool for harmonic analysis and structure definition of data: Multiscale methods, *Proc. Natl. Acad. Sci. USA* **102**, 7432 (2005).
- [108] R. R. Coifman and S. Lafon, Diffusion maps, *Appl. Comput. Harmon. Anal.* **21**, 5 (2006).
- [109] Note that for the diffusion map approach, two samples far from each other may have considerable diffusion probability with the assistance of symmetry, as discussed in Ref.[94]. However, in this work we do not assume that the model Hamiltonian has certain symmetry and thus the effect of symmetries will not be discussed for simplicity.
- [110] See Supplemental Material at [URL will be inserted by publisher] for details on the introduction of diffusion map, non-Hermitian topological phases of matter, theoretical analysis and more numerical calculations of clustering results.
- [111] E. J. Bergholtz, J. C. Budich, and F. K. Kunst, Exceptional topology of non-hermitian systems, *arXiv:1912.10048* (2019).
- [112] K. Zhang, Z. Yang, and C. Fang, Correspondence between Winding Numbers and Skin Modes in Non-Hermitian Systems, *Phys. Rev. Lett.* **125**, 126402 (2020).
- [113] A. Kitaev, Periodic table for topological insulators and superconductors, *AIP Conf. Proc.* **1134**, 22 (2009).
- [114] Here for simplicity, we did not take into account the effect of symmetry in phase clustering. In diffusion map algorithm, two samples far from each other may have considerable diffusion probability with the assistance of symmetry. For details, see *PRL.124.226401*.
- [115] For non-Hermitian topological systems with PBC, there also exist gapless phases. For example, the 2D non-Hermitian Qi-Wu-Zhang(QWZ) model has gapless phases.

## Supplementary Material for: Unsupervised Learning of Non-Hermitian Topological Phases

Diffusion map is a sort of typical manifold learning algorithm [106–108], which provides non-linear dimensionality reduction and unsupervised clustering of raw data without any priori knowledge. It combines the heat diffusion with the random walk Markov chain. Concretely, given a set of input data  $\mathbf{x} = \{\mathbf{x}^{(1)}, \mathbf{x}^{(2)}, \dots, \mathbf{x}^{(L)}\}$ , where  $\mathbf{x}^{(i)}$  represents the  $i$ -th data point in complex space  $\mathbb{C}^d$ . The connectivity between two points  $\mathbf{x}^{(l)}$  and  $\mathbf{x}^{(l')}$  is described by the local similarity, which is required to be positive definite and symmetric. For example, the Gaussian kernel

$$\mathcal{K}_{l,l'} = \exp\left(-\frac{\|\mathbf{x}^{(l)} - \mathbf{x}^{(l')}\|_{\mathbb{L}_p}^2}{2\epsilon}\right), \quad (\text{S1})$$

where  $\|\mathbf{x}^{(l)} - \mathbf{x}^{(l')}\|_{\mathbb{L}_p}$  represents the  $\mathbb{L}_p$ -norm distance between two points  $\mathbf{x}^{(l)}$  and  $\mathbf{x}^{(l')}$ , variance  $\epsilon$  is a small quantity to be adjusted. Recently, applications of  $p = 1, 2, \infty$  cases in unsupervised clustering topological phases have been reported [93–96]. When  $p = 2$ , the distance is the familiar Euclidean distance. With such kernel, the one-step transition matrix  $\mathcal{P}$  of Markovian random walk between two points  $\mathbf{x}^{(l)}$  and  $\mathbf{x}^{(l')}$  can be defined as follows

$$\mathcal{P}_{l,l'} = \frac{\mathcal{K}_{l,l'}}{\sum_{l'} \mathcal{K}_{l,l'}}, \quad (\text{S2})$$

where  $\mathcal{P}_{l,l'}$  obeys the probability conservation condition  $\sum_l \mathcal{P}_{l,l'} = 1$ . Then after  $2t$  steps of random walk, the connectivity between  $\mathbf{x}^{(l)}$  and  $\mathbf{x}^{(l')}$  is given by the diffusion distance

$$D_t(l, l') = D_t(\mathbf{x}^{(l)}, \mathbf{x}^{(l')}) = \sum_{k=1}^L \frac{(\mathcal{P}_{l,k}^t - \mathcal{P}_{l',k}^t)^2}{\sum_j \mathcal{K}_{k,j}} = \sum_{k=1}^{L-1} \lambda_k^{2t} [(\psi_k)_l - (\psi_k)_{l'}]^2 \geq 0, \quad (\text{S3})$$

where  $\{\psi_k\}$  are the right eigenvectors of  $\mathcal{P}$ ,  $\mathcal{P}\psi_k = \lambda_k\psi_k$ ,  $k = 0, 1, \dots, L-1$ , the corresponding eigenvalues rank in descending order, i.e.  $\lambda_0 = 1 \geq \lambda_1 \geq \dots \geq \lambda_{L-1}$ .  $k = 0$  term does not contribute because the corresponding right eigenvector is constant with all vector elements equivalent.

Under the mapping

$$\mathbf{x}^{(l)} \rightarrow \Psi_t^{(l)} := [\lambda_1^t (\psi_1)_l, \lambda_2^t (\psi_2)_l, \dots, \lambda_{L-1}^t (\psi_{L-1})_l], \quad (\text{S4})$$

the distance between samples  $\mathbf{x}^{(l)}$  and  $\mathbf{x}^{(l')}$  can be recast as the Euclidean distance in  $\Psi$  space

$$D_t(\mathbf{x}^{(l)}, \mathbf{x}^{(l')}) = \|\Psi_l - \Psi_{l'}\|_{\mathbb{L}_2}^2. \quad (\text{S5})$$

After  $t \rightarrow \infty$  steps, only the first few components with largest  $|\lambda_k| \approx 1$  are dominant due to the term  $\lambda_k^t$  in  $\Psi_t$ . Hence almost all the distance information is encoded in such few components. Then the original samples  $\mathbf{x}^{(l)}$  with higher dimension are reduced to the lower ones, and the clustering method (e.g.  $k$ -means) can be applied in  $\Psi$  space to cluster the corresponding samples with no prior knowledge. Specifically, in clustering the topological phases of quantum models, the number of  $|\lambda_k| \approx 1$  equals to the number of topological clusters without prior labels. Hence it is possible for such algorithm to detect unknown topological phases.

### PHASES OF NON-HERMITIAN TOPOLOGICAL MODELS

#### 1D non-Hermitian Su-Schrieffer-Heeger model

*Periodic boundary condition*

With periodic boundary condition(PBC), the system obeys translational symmetry, and the bulk Hamiltonian takes the form

$$\hat{H}_p^{1D}(k) = \vec{\mathbf{d}} \cdot \boldsymbol{\sigma} = d_x \sigma_x + d_y \sigma_y \quad (\text{S6})$$

in the momentum bases  $\{C_{k,A}, C_{k,B}\}$ , where  $C_{k,A}$  and  $C_{k,B}$  represent the fermionic sublattice sites,  $\vec{\mathbf{d}} = (d_x, d_y)$ ,  $d_x = t_1 + t_2 \cos k$ ,  $d_y = t_2 \sin k + i\gamma$ . The 1D Brillouin zone is given by  $[-\pi, \pi]$ . Winding number  $W = \frac{1}{\pi} \int_{-\pi}^{\pi} \frac{d_x \partial_k d_y - d_y \partial_k d_x}{d_x^2 + d_y^2} dk$



counts the times of the mapping wrapping around the original point. Different winding numbers indicate different topological phases of matter:

$$W = \begin{cases} 0, & |t_1 \pm \gamma| > |t_2|; \\ \frac{1}{2}, & |t_1 \pm \gamma| < |t_2| \& |\gamma| > |t_2|; \\ 1, & |t_1 \pm \gamma| < |t_2| \& |\gamma| < |t_2|. \end{cases} \quad (\text{S7})$$

The above half-winding number has a geometrical explanation, see Ref. [27] for details. For the non-Hermitian system with PBC, the sublattice symmetry [29]  $\mathcal{S} = \sigma_z, \sigma_z \hat{H}_p^{(1D)}(k) \sigma_z = -\hat{H}_p^{(1D)}(k)$  ensures that the bulk bands are in pairs  $E_{\pm}(k) = \pm \sqrt{(t_1 + t_2 \cos k)^2 + (t_2 \sin k + i\gamma)^2}$ . The topological phase transition occurs at the exceptional points  $t_1 = -t_2 \pm \gamma$  ( $k = 0$ ) and  $t_1 = t_2 \pm \gamma$  ( $k = \pi$ ), which coincide with the change of winding numbers.

#### Open boundary condition

The 1D non-Hermitian SSH model in the real space takes the following form:

$$\hat{H}_o^{1D} = \sum_{i=1}^N (t_1 + \gamma) C_{i,A}^\dagger C_{i,B} + (t_1 - \gamma) C_{i,B}^\dagger C_{i,A} + t_2 C_{i,B}^\dagger C_{i+1,A} + t_2 C_{i+1,A}^\dagger C_{i,B}. \quad (\text{S8})$$

With OBC, the conventional bulk-boundary correspondence (BBC) breaks down, and the non-Hermitian skin effect arises. Theoretically, one straightforward method of detecting the topological phase transition is to calculate its ground state degeneracy. Direct numerical calculation of Eq. (S8) with a large enough chain length shows that the 2-fold ground state degeneracy holds in the interval  $|t_1| < \sqrt{t_2^2 + \gamma^2}$ . Hence the phase transition occurs at  $t_1 = \pm \sqrt{t_2^2 + \gamma^2}$ . This phase boundary does no longer correspond to the exceptional point in Brillouin zone, but one can reconstruct the generalized BBC based on a similarity transformation  $\Gamma$  on the Hamiltonian matrix represented in bases  $\{C_{1,A}, C_{1,B}, C_{2,A}, \dots, C_{N,B}\}^T$ ,

$$\bar{H}_o^{1D} = \Gamma^{-1} \hat{H}_o^{1D} \Gamma, \quad (\text{S9})$$

where  $\Gamma$  is a  $2N \times 2N$  diagonal matrix with the diagonal elements  $\{1, r, r, r^2, r^2, \dots, r^{N-1}, r^{N-1}, r^N\}$ , and  $r = \sqrt{|(t_1 - \gamma)/(t_1 + \gamma)|}$ . Then the non-Hermitian matrix  $\hat{H}_o^{1D}$  is transformed into a Hermitian matrix  $\bar{H}_o^{1D}$  by  $S$ , with the trade-off that the bases are transformed to be non-orthonormal as  $\{C_{1,A}, r^{-1}C_{1,B}, r^{-1}C_{2,A}, \dots, r^{-N}C_{N,B}\}^T$ . When  $|t_1| > |\gamma|$ , i.e.  $r$  is real, the Hermitian  $\bar{H}_o^{1D}$  is exactly the SSH matrix. Fourier transformation maps the real space SSH matrix  $\bar{H}_o^{1D}$  to the momentum space,

$$\bar{H}_o^{1D}(k) = (\bar{t}_1 + t_2 \cos k) \sigma_x + t_2 \sin k \sigma_y, \quad \bar{t}_1 = \sqrt{(t_1 + \gamma)(t_1 - \gamma)}. \quad (\text{S10})$$

Clearly, the topological phase transition of  $\bar{H}_o^{1D}(k)$  occurs at  $|\bar{t}_1| = |t_2|$ , i.e.  $t_1 = \pm \sqrt{t_2^2 + \gamma^2}$ , with the change of topological winding numbers. Hence to discuss the BBC for such non-Hermitian model, one approach is to transform it into the Hermitian matrix formalism under the similarity transformation.

Another equivalent approach to define the non-Hermitian BBC is to introduce the concept of generalized Brillouin zone  $H(e^{ik} \rightarrow \beta)$ , which transforms the Bloch phase factor  $e^{ik}$  into  $|\beta| \neq 1$  for the non-Hermitian case,

$$e^{ik} := \beta = \sqrt{\frac{t_1 - \gamma}{t_1 + \gamma}} e^{iq}, \quad q \in \mathbb{R}. \quad (\text{S11})$$

Under such transformation, the matrix form of  $H'(\beta)$  in generalized Brillouin zone is exactly the same as Eq. (S10). Then the generalized BBC holds.

## 2D non-Hermitian Qi-Wu-Zhang model

#### Periodic boundary condition

The non-Hermitian Qi-Wu-Zhang (QWZ) model takes the following form [42],

$$\hat{H}^{2D} = \left[ \sum_{\mathbf{y}} \sum_{j=x,y} c_{\mathbf{y}}^\dagger \left( -\frac{i}{2} v_j \sigma_j - \frac{1}{2} t_j \sigma_z \right) c_{\mathbf{y} + \mathbf{e}_j} + h.c. \right] + \sum_{\mathbf{y}} c_{\mathbf{y}}^\dagger (M \sigma_z + i \sum_{j=x,y,z} \gamma_j \sigma_j) c_{\mathbf{y}}, \quad (\text{S12})$$

where  $c_{\mathbf{y}} = (c_{\mathbf{y},A}, c_{\mathbf{y},B})^T$  represents the unit cell fermionic annihilation operator,  $\mathbf{y}$  labels the 2D lattice number of the unit cell, and  $\mathbf{e}_j$  is the unit vector in  $j = x, y$  directions. Here we also consider two types of boundary conditions: PBC and OBC.

With PBC, the non-Hermitian QWZ model in Eq. (S12) is Fourier transformed into the bulk Hamiltonian in Brillouin zone,

$$\begin{aligned} H_p(\mathbf{k}) &= \vec{\mathbf{d}} \cdot \vec{\sigma} = d_x \sigma_x + d_y \sigma_y + d_z \sigma_z \\ &= (v_x \sin k_x + i\gamma_x) \sigma_x + (v_y \sin k_y + i\gamma_y) \sigma_y \\ &\quad + (M - t_x \cos k_x - t_y \cos k_y + i\gamma_z) \sigma_z. \end{aligned} \quad (\text{S13})$$

For simplicity, let  $\gamma_z = 0$ ,  $t_x = t_y = 0.5$ , then the theoretical phase transition boundaries are

$$\begin{aligned} M_{\pm}^{(1)} &= 1 \pm \sqrt{\gamma_x^2 + \gamma_y^2} \quad (k_x, k_y) = (0, 0), \\ M_{\pm}^{(2)} &= \pm \sqrt{\gamma_x^2 + \gamma_y^2} \quad (k_x, k_y) = (0, \pi), (\pi, 0), \\ M_{\pm}^{(3)} &= -1 \pm \sqrt{\gamma_x^2 + \gamma_y^2} \quad (k_x, k_y) = (\pi, \pi), \end{aligned} \quad (\text{S14})$$

One unique feature of such model is that in regions  $M \in (M_{-}^{(\nu)}, M_{+}^{(\nu)})$  for  $\nu = 1, 2, 3$  the Hamiltonian is gapless and the topological indices are not well-defined in these regions.

#### Open boundary condition

With OBC, the conventional BBC breaks down. We have to consider the influence of non-Hermitian skin effect. In OBC (independent of the geometrical configuration, such as square or disk, *etc.* [42]), it has been shown from both the analytical and numerical aspects that one topological phase boundary is approximately expressed as

$$M = t_x + t_y + \frac{t_x \gamma_x^2}{2v_x^2} + \frac{t_y \gamma_y^2}{2v_y^2} \quad (\text{S15})$$

for small  $\frac{\gamma_{x(y)}}{v_{x(y)}}$ . When  $M < t_x + t_y + \frac{t_x \gamma_x^2}{2v_x^2} + \frac{t_y \gamma_y^2}{2v_y^2}$ , the corresponding Chern number in generalized Brillouin zone for the valence band ( $\text{Re}(E) < 0$ ) is  $C = 1$ . While for  $M > t_x + t_y + \frac{t_x \gamma_x^2}{2v_x^2} + \frac{t_y \gamma_y^2}{2v_y^2}$ , the topological index is  $C = 0$ . Hence the boundary separates the system into two distinct topological regions. For more details, see Ref. [42].

## THE APPLICABILITY OF DIFFUSION MAP IN NON-HERMITIAN TOPOLOGICAL PHASE TRANSITION

Here we theoretically analyze the applicability of diffusion map in classifying the non-Hermitian topological phases.

#### Periodic boundary condition

With PBC, the 2-level topological band model reads

$$\hat{H} = \vec{\mathbf{d}} \cdot \vec{\sigma} = d_x \sigma_x + d_y \sigma_y + d_z \sigma_z \quad (\text{S16})$$

with the free fermionic bases  $\{C_{\mathbf{k},A}, C_{\mathbf{k},B}\}$ , where  $\{d_x, d_y, d_z\}$  can be complex for the non-Hermitian model, the corresponding energy levels  $E_{\pm} = \pm \sqrt{d_x^2 + d_y^2 + d_z^2}$ . Then the Hamiltonian are equivalently described by the vector  $\vec{\mathbf{d}}$  in Pauli space. In the  $d$ -dimensional lattice model, the momentum vectors  $\mathbf{k}$  are discrete in Brillouin zone  $[-\pi, \pi]^d$ . To apply the diffusion map algorithm to such models, the vectors  $\hat{\mathbf{d}} = \frac{\vec{\mathbf{d}}}{\sqrt{d_x^2 + d_y^2 + d_z^2}}$  are chosen as the raw data, e.g. for the 1D model with length  $N$ , the data sample  $\mathbf{x}^{(l)} = \{\hat{\mathbf{d}}(k_i), |k_i = \frac{2i-N-2}{N}\pi, i \in [1, N]\}$ . By varying the parameters  $\vec{t} = (t_1, t_2, \dots)$  in  $\hat{\mathbf{d}}$ , one obtains the data set  $\{\mathbf{x}^{(l)}\}$ .

In our diffusion map algorithm, the diffusion probability  $\mathcal{P}_{l,l'} = \frac{\mathcal{K}_{l,l'}}{\sum_{l'} \mathcal{K}_{l,l'}}$  between samples  $\mathbf{x}^{(l)}$  and  $\mathbf{x}^{(l')}$  is defined by choosing the Gaussian kernel function with the  $\mathbb{L}_1$ -norm

$$\mathcal{K}_{l,l'} = \exp\left(-\frac{\|\mathbf{x}^{(l)} - \mathbf{x}^{(l')}\|_{\mathbb{L}_1}^2}{2\epsilon N^2}\right), \quad (\text{S17})$$

where the variance is controlled by  $0 < \epsilon \ll 1$ .

Importantly, without the assistance of symmetric operators [114], it is easy to find that the prominent contributions of the one-step diffusion probability  $P_{l,l'}$  are from those nearest samples  $l' = l + \delta l$ , i.e. the corresponding parameters  $\vec{t}' = \vec{t} + \delta \vec{t}$ , then the  $\mathbb{L}_1$ -norm distance between  $l$  and  $l + \delta l$  can be approximately recast to

$$\|\mathbf{x}^{(l)} - \mathbf{x}^{(l+\delta l)}\|_{\mathbb{L}_1} = \sum_{i=1}^N \sum_{\alpha=x,y,z} \left( \|\hat{d}_\alpha^{(l)}(k_i) - \hat{d}_\alpha^{(l+\delta l)}(k_i)\|_{\mathbb{L}_1} \right) \approx \sum_{i=1}^N \sum_{\alpha=x,y,z} \left( \|\nabla_{\vec{t}}(\hat{d}_\alpha^{(l)}(k_i))\|_{\mathbb{L}_1} \right) \cdot \delta \vec{t}. \quad (\text{S18})$$

Then the Gaussian kernel  $\mathcal{K}_{l,l+\delta l}$  reads

$$\mathcal{K}_{l,l+\delta l} \approx \exp \left( -\frac{\left( \sum_{i=1}^N \sum_{\alpha=x,y,z} \left( \|\nabla_{\vec{t}}(\hat{d}_\alpha^{(l)}(k_i))\|_{\mathbb{L}_1} \right) \cdot \delta \vec{t} \right)^2}{2\epsilon N^2} \right). \quad (\text{S19})$$

In case of confusion, we note that  $\|\nabla_{\vec{t}} \hat{\mathbf{d}}\|_{\mathbb{L}_1} = \left( \|\partial_{t_1} \hat{\mathbf{d}}\|_{\mathbb{L}_1}, \|\partial_{t_2} \hat{\mathbf{d}}\|_{\mathbb{L}_1}, \dots, \|\partial_{t_n} \hat{\mathbf{d}}\|_{\mathbb{L}_1} \right)$ .

As long as  $\sum_{i=1}^N \left( |\nabla_{\vec{t}}(\hat{d}_x^{(l)}(k_i))| + |\nabla_{\vec{t}}(\hat{d}_y^{(l)}(k_i))| + |\nabla_{\vec{t}}(\hat{d}_z^{(l)}(k_i))| \right)$  is finite, the constant  $\delta \vec{t}^2 / \epsilon$  can always be adjusted so as to keep  $\mathcal{K}_{l,l+\delta l} \approx 1$ . Hence the connectivity between  $l$  and  $l'$  depends on the derivability of the vector  $\hat{\mathbf{d}}^{(l)} = \frac{\vec{\mathbf{d}}}{\sqrt{d_x^2 + d_y^2 + d_z^2}} = \frac{\mathbf{d}^{(l)}}{E_+^{(l)}}$

on  $\vec{t}$  for all  $k_i \in [-\pi, \pi]$ . The gap closure points  $E_\pm^{(l)} = 0$  usually break the constraint. Hence two nearest data samples divided by the gap closure point should have  $\mathcal{K}_{l,l'} \approx 0$ , i.e. no one-step diffusion probability between such samples. Combined with the approximation that only the nearest samples prominently contribute to the diffusion, as a consequence, the gap closure points divide the diffusion matrix into blocks. In most cases, different blocks usually correspond to different topological phases both for Hermitian and non-Hermitian cases [115].

**Example: 1D non-Hermitian SSH model with PBC.**— For illustration, we focus on the 1D non-Hermitian SSH model with PBC

$$H_p(k) = \vec{\mathbf{d}} \cdot \vec{\sigma} = d_x \sigma_x + d_y \sigma_y, \quad d_x = t_1 + t_2 \cos k, \quad d_y = t_2 \sin k + i\gamma. \quad (\text{S20})$$

The data set  $\{\mathbf{x}^{(l)} | \mathbf{x}^{(l)} = \{\hat{\mathbf{d}}(k_i), |k_i = \frac{2i-N-2}{N}\pi, i \in [1, N]\}\}$  for clustering is obtained by varying only one parameter  $t_1$ , while fixing  $t_2$  and the non-Hermitian term  $\gamma$ . Correspondingly, the  $\mathbb{L}_1$ -norm term in Eq. (S18) reads

$$\frac{\|\mathbf{x}^{(l)} - \mathbf{x}^{(l+\delta l)}\|_{\mathbb{L}_1}}{\delta t_1} \approx \sum_{i=1}^N \left( |\partial_{t_1}(\hat{d}_x^{(l)}(k_i))| + |\partial_{t_1}(\hat{d}_y^{(l)}(k_i))| \right) = \sum_{i=1}^N \left( \left| \frac{d_y^{(l)2}}{E_+^{(l)3}} \right|_{k_i} + \left| \frac{d_x^{(l)} d_y^{(l)}}{E_+^{(l)3}} \right|_{k_i} \right). \quad (\text{S21})$$

It is easy to verify that Eq. (S21) tends to be infinite at the gap closure points  $E_\pm = 0$ , i.e. the critical cases  $t_1 = t_2 \pm \gamma$  ( $k_i = -\pi$ ) and  $t_1 = -t_2 \pm \gamma$  ( $k_i = 0$ ). Hence the kernel value  $\mathcal{K}_{l,l+\delta l} \approx 0$  around such points and the kernel matrix becomes block diagonal. As a consequence, the diffusion map algorithm successfully classifies the topological phases of the 1D non-Hermitian SSH model with PBC.

### Open boundary condition

Here we show how to apply the diffusion map method to classify phases of non-Hermitian topological models with OBC.

For the case of OBC, the raw data is no longer the Hamiltonian vector in momentum space. Instead, we choose the real space projective matrix elements as the raw data. Generally, a projective matrix of such topological model is defined as

$$P = \sum_{\text{Re}[E_m] < 0} |m_R\rangle \langle m_L|, \quad (\text{S22})$$

where  $|m_R\rangle$  and  $\langle m_L|$  are the right and left eigenstates of the non-Hermitian model,  $m$  covers the continuum bulk spectrum leaving out the discrete zero modes.

We reiterate that the diffusion between the nearest samples contributes prominently. To illustrate the applicability of the diffusion map method in clustering real space data samples, we consider the projective matrix  $P^{(l+\delta l)} = P(\vec{t}^{(l+\delta l)})$  in first-order perturbation

$$P^{(l+\delta l)} = \sum_{\text{Re}[E_m] < 0} |m'_R\rangle \langle m'_L| \approx \sum_{\text{Re}[E_m] < 0} \left( |m_R\rangle + \sum_{n \neq m} \frac{\langle n_L | \delta \hat{H} | m_R \rangle}{E_m - E_n} |n_R\rangle \right) \left( \langle m_L| + \sum_{n \neq m} \frac{\langle m_L | \delta \hat{H} | n_R \rangle}{E_m - E_n} \langle n_L| \right), \quad (\text{S23})$$

where  $\delta\hat{H} = \hat{H}^{(l+\delta l)} - \hat{H}^{(l)}$  and then

$$\delta P = P^{(l+\delta l)} - P^{(l)} = \sum_{\substack{\text{Re}[E_m] < 0 \\ n \neq m}} (|m'_R\rangle\langle m'_L| - |m_R\rangle\langle m_L|) \approx \sum_{\substack{\text{Re}[E_m] < 0 \\ n \neq m}} \left( \frac{\langle n_L | \delta\hat{H} | m_R \rangle}{E_m - E_n} |n_R\rangle\langle m_L| + \frac{\langle m_L | \delta\hat{H} | n_R \rangle}{E_m - E_n} |m_R\rangle\langle n_L| \right). \quad (\text{S24})$$

Hence the Gaussian kernel can be reexpressed as

$$\mathcal{K}_{l,l+\delta l} = \exp\left(-\frac{\|P^{(l)} - P^{(l+\delta l)}\|_{\mathbb{L}_1}^2}{2\epsilon N^2}\right) = \exp\left(-\frac{\|\delta P\|_{\mathbb{L}_1}^2}{2\epsilon N^2}\right) = \exp\left(-\frac{(\|\nabla_{\vec{t}} P\|_{\mathbb{L}_1} \cdot \delta\vec{t})^2}{2\epsilon N^2}\right), \quad (\text{S25})$$

where  $\|\nabla_{\vec{t}} P\|_{\mathbb{L}_1} = (\|\partial_{t_1} P\|_{\mathbb{L}_1}, \|\partial_{t_2} P\|_{\mathbb{L}_1}, \dots, \|\partial_{t_n} P\|_{\mathbb{L}_1})$ . The singularity of  $\|\nabla_{\vec{t}} P\|_{\mathbb{L}_1}$  is crucial to the kernel values.

**Example: 1D non-Hermitian SSH model with OBC.**– Now we take the 1D non-Hermitian SSH model in Eq. (S8) as an example. The data set  $\{\mathbf{x}^{(l)}\}$  is obtained by varying  $t_1$ . It is well known that the non-Hermitian SSH matrix  $\hat{H}_o^{1D}$  in the orthonormal bases can be transformed into a Hermitian SSH matrix  $\bar{H}_o^{1D}$  in the non-orthonormal bases for  $|t_1| > |\gamma|$ ,

$$\bar{H}_o^{1D} = \Gamma^{-1} \hat{H}_o^{1D} \Gamma, \quad \Gamma^{-1}|n\rangle = |n_R\rangle, \quad \langle n|\Gamma = \langle n_L|, \quad \bar{H}_o^{1D}|n\rangle = E_n|n\rangle. \quad (\text{S26})$$

where  $\Gamma = \text{Diag}(1, r, r, r^2, r^2, \dots, r^{N-1}, r^N)$ ,  $r = \sqrt{|(t_1 - \gamma)/(t_1 + \gamma)|}$ . Then the term  $\|\nabla_{\vec{t}} P\|_{\mathbb{L}_1}$  can be expressed as

$$\begin{aligned} \|\nabla_{\vec{t}} P\|_{\mathbb{L}_1} &= \|\partial_{t_1} P\|_{\mathbb{L}_1} = \left\| \sum_{\substack{\text{Re}[E_m] < 0 \\ n \neq m}} \left( \frac{\langle n_L | \partial_{t_1} \hat{H}_o^{1D} | m_R \rangle}{E_m - E_n} |n_R\rangle\langle m_L| + \frac{\langle m_L | \partial_{t_1} \hat{H}_o^{1D} | n_R \rangle}{E_m - E_n} |m_R\rangle\langle n_L| \right) \right\|_{\mathbb{L}_1} \\ &= \left\| \sum_{\substack{\text{Re}[E_m] < 0 \\ n \neq m}} \left( \frac{\langle n | \Gamma \partial_{t_1} \hat{H}_o^{1D} \Gamma^{-1} | m \rangle}{E_m - E_n} \Gamma^{-1}|n\rangle\langle m| \Gamma + \frac{\langle m | \Gamma \partial_{t_1} \hat{H}_o^{1D} \Gamma^{-1} | n \rangle}{E_m - E_n} \Gamma^{-1}|m\rangle\langle n| \Gamma \right) \right\|_{\mathbb{L}_1}. \end{aligned} \quad (\text{S27})$$

Here for convenience, we calculate the  $\mathbb{L}_1$ -norm in the fermionic bases  $\{C_{1,A}, C_{1,B}, C_{2,A}, \dots, C_{N,B}\}$  instead of the eigenstate bases  $\{|n\rangle\}$  of  $\bar{H}$ . Similar to the Hermitian SSH model, the singularity of  $\|\nabla_{\vec{t}} P\|_{\mathbb{L}_1}$  still occurs in condition  $|E_{-1} - E_1| \rightarrow 0$ , which corresponds to the phase transition points  $|t_1| = \sqrt{t_2^2 + \gamma^2}$ . In the next section, we show in detail that the terms  $\frac{\langle 1 | \Gamma \partial_{t_1} \hat{H} \Gamma^{-1} | -1 \rangle}{E_{-1} - E_1}$  and  $\frac{\langle -1 | \Gamma \partial_{t_1} \hat{H} \Gamma^{-1} | 1 \rangle}{E_{-1} - E_1}$  are both infinite, while all other associated parameters are finite. Here to remove the possible exponential infinity of NHSE, we choose part of the  $P$ -matrix elements as the raw input data:  $\{P_{iA, iB} | i \in [1, N]\}$ , i.e. the parameters of  $C_{i,B}^\dagger C_{i,A}$ -terms in  $\Gamma^{-1}|-1\rangle\langle 1|\Gamma$  and  $\Gamma^{-1}|1\rangle\langle -1|\Gamma$  are finite numbers  $\pm r$ . Hence for each matrix element  $P_{iA, iB}$ , the value of the  $\mathbb{L}_1$ -norm tends to be infinite near the phase transition points  $|t_1| = \sqrt{t_2^2 + \gamma^2}$ . As a consequence, the corresponding Gaussian kernel value tends to be zero, and there is not diffusion probability between the two samples in different phases. It indicates the applicability of the diffusion map algorithm in non-Hermitian model with OBC.

#### DETAILED CALCULATIONS OF $\langle n | \Gamma \partial_{t_1} \hat{H}_o^{1D} \Gamma^{-1} | m \rangle / N$ IN 1D NON-HERMITIAN SSH MODEL

To manifest that the only singularity originates from the gap closure, we need to show that the term  $\langle n | \Gamma \partial_{t_1} \hat{H}_o^{1D} \Gamma^{-1} | m \rangle / N$  is finite for all bulk eigenstates  $\{|n\rangle\}$  of the 1D non-Hermitian SSH model ( $|t_1| > |\gamma|$ ) with OBC in Eq. (S8).

In single fermion system, the eigenstate  $|n\rangle$  can be expressed as  $|n\rangle = \sum_i (u_{ni}^A C_{i,A}^\dagger + u_{ni}^B C_{i,B}^\dagger) |\text{Vac}\rangle$ ,  $\sum_i (|u_{ni}^A|^2 + |u_{ni}^B|^2) = 1$ . Then the term  $\langle n | \Gamma \partial_{t_1} \hat{H}_o^{1D} \Gamma^{-1} | m \rangle / N$  takes the form

$$\begin{aligned} \frac{1}{N} \langle n | \Gamma \partial_{t_1} \hat{H}_o^{1D} \Gamma^{-1} | m \rangle &= \frac{1}{N} \sum_{i=1}^N \langle n | (r C_{i,A}^\dagger C_{i,B} + r^{-1} C_{i,B}^\dagger C_{i,A}) | m \rangle, \\ &= \frac{1}{N} \sum_{i=1}^N r (u_{ni}^A)^* u_{mi}^B + r^{-1} (u_{ni}^B)^* u_{mi}^A \end{aligned} \quad (\text{S28})$$

which is of order  $r^{\pm 1}$ . Hence the term  $\langle n|\Gamma\partial_{t_1}\hat{H}_o^{1D}\Gamma^{-1}|m\rangle/N$  is finite for finite  $r$ .

Then we focus on the singularity of the term  $\frac{\langle -1|\Gamma\partial_{t_1}\hat{H}_o^{1D}\Gamma^{-1}|1\rangle\langle 1|\Gamma+(1|\Gamma\partial_{t_1}\hat{H}_o^{1D}\Gamma^{-1}|1)\Gamma^{-1}|1\rangle\langle -1|\Gamma}{N(E_{-1}-E_1)}$ . Let the system be initially in topological trivial phase. Without loss of generality, we suppose the chain length  $N$  is large enough, and the lowest excitation (annihilation) energy  $E_1(E_{-1})$  of  $\hat{H}_o^{1D}$  with OBC is almost equivalent to that of  $\bar{H}_o^{1D}(k)$  with PBC, and the corresponding eigenstates can be approximately expressed by

$$|\pm 1\rangle \approx \bar{C}_{k_0,A(B)}^\dagger|\text{Vac}\rangle$$

for large  $N$ , where  $k_0$  corresponds to the lowest excitation momentum of  $\bar{H}_o^{1D}(k)$  with PBC in Eq. (S10). By diagonalizing  $\bar{H}_o^{1D}$  with Fourier transformation in the momentum bases  $\{C_{k,A}^\dagger, C_{k,B}^\dagger\}$ , one obtains

$$\bar{H}_k = \sum_{k=-\pi}^{\pi} E_k \bar{C}_{k,A}^\dagger \bar{C}_{k,A} - E_k \bar{C}_{k,B}^\dagger \bar{C}_{k,B}, \quad C_{k,A(B)}^\dagger = \frac{1}{\sqrt{N}} \sum_{j=1}^N e^{-ikj} C_{j,A(B)}^\dagger, \quad (\text{S29})$$

where  $\bar{C}_{k,A}^\dagger = \frac{1}{\sqrt{2}}(\xi_k C_{k,A}^\dagger + C_{k,B}^\dagger)$  and  $\bar{C}_{k,B}^\dagger = \frac{1}{\sqrt{2}}(-\xi_k^* C_{k,A}^\dagger + C_{k,B}^\dagger)$  are the fermionic quasiparticle operators,  $\xi_k = \sqrt{(\bar{t}_1 + t_2 e^{-ik})/(\bar{t}_1 + t_2 e^{ik})}$  is just a phase for real  $\bar{t}_1$  in Eq. (S10).

We first estimate the value of the term  $\langle -1|\Gamma\partial_{t_1}\hat{H}_o^{1D}\Gamma^{-1}|1\rangle/N$ ,

$$\begin{aligned} & \frac{1}{N} \langle -1|\Gamma\partial_{t_1}\hat{H}_o^{1D}\Gamma^{-1}|1\rangle \\ &= \frac{1}{2N} \sum_{k=-\pi}^{\pi} \langle \text{Vac}|\bar{C}_{k_0,B} \left( \left( \frac{r}{\xi_k} + \frac{\xi_k}{r} \right) (\bar{C}_{k,A}^\dagger \bar{C}_{k,A} - \bar{C}_{k,B}^\dagger \bar{C}_{k,B}) + \left( \frac{r}{\xi_k} - \frac{\xi_k}{r} \right) (\bar{C}_{k,A}^\dagger \bar{C}_{k,B} - \bar{C}_{k,B}^\dagger \bar{C}_{k,A}) \right) \bar{C}_{k_0,A}^\dagger |\text{Vac}\rangle \\ &= \frac{1}{2N} \left( \frac{\xi_{k_0}}{r} - \frac{r}{\xi_{k_0}} \right). \end{aligned} \quad (\text{S30})$$

Correspondingly, the term  $\langle 1|\Gamma\partial_{t_1}\hat{H}_o^{1D}\Gamma^{-1}|1\rangle/N = \frac{1}{2N} \left( \frac{r}{\xi_{k_0}} - \frac{\xi_{k_0}}{r} \right)$ .

Then we analyze the singularity of the term  $\Gamma^{-1}|1\rangle\langle 1|\Gamma$ . Recalling the definition of the  $\mathbb{L}_1$ -norm for the matrix  $\|P\|_{\mathbb{L}_1} = \sum_{i,j} |P_{ij}|$ , here we choose the fermionic bases in real space  $\{C_{1,A}, C_{1,B}, C_{2,A}, \dots, C_{N,B}\}$ . The term can be expressed as

$$\Gamma^{-1}|1\rangle\langle 1|\Gamma = \Gamma^{-1} \bar{C}_{k_0,B}^\dagger |\text{Vac}\rangle \langle \text{Vac}|\bar{C}_{k_0,A} \Gamma = \frac{1}{2} \Gamma^{-1} (-\xi_{k_0}^* C_{k_0,A}^\dagger + C_{k_0,B}^\dagger) |\text{Vac}\rangle \langle \text{Vac}|(\xi_{k_0}^* C_{k_0,A} + C_{k_0,B}) \Gamma. \quad (\text{S31})$$

It is easy to find that in the fermionic bases,  $\Gamma$ -matrix would contribute the exponential infinite term  $\sim r^N$ , hence we choose the element set  $\{C_{i,A}^\dagger|\text{Vac}\rangle\langle \text{Vac}|C_{i,B}|i \in [1, N]\}$  as the raw data instead of the full projective matrix  $P$  to overcome the obstacle. In  $\Gamma^{-1}|1\rangle\langle 1|\Gamma$ , the term  $C_{i,A}^\dagger|\text{Vac}\rangle\langle \text{Vac}|C_{i,B}$  has parameter  $-\frac{\xi_{k_0}^* r}{2N}$ , while in  $\Gamma^{-1}|1\rangle\langle -1|\Gamma$ , the  $C_{i,A}^\dagger|\text{Vac}\rangle\langle \text{Vac}|C_{i,B}$  has parameter  $\frac{\xi_{k_0}^* r}{2N}$ . Thus for each matrix element  $C_{i,A}^\dagger|\text{Vac}\rangle\langle \text{Vac}|C_{i,B}$ , the total parameter contributed from the two energy levels  $E_{\pm 1}$  is

$$\begin{aligned} & \frac{\langle -1|\Gamma\partial_{t_1}\hat{H}_o^{1D}\Gamma^{-1}|1\rangle\langle 1|\Gamma+(1|\Gamma\partial_{t_1}\hat{H}_o^{1D}\Gamma^{-1}|1)\Gamma^{-1}|1\rangle\langle -1|\Gamma}{N(E_{-1}-E_1)} \Bigg|_{C_{i,A}^\dagger|\text{Vac}\rangle\langle \text{Vac}|C_{i,B}} \\ &= \frac{-\frac{\xi_{k_0}^* r}{2N} \langle -1|\Gamma\partial_{t_1}\hat{H}_o^{1D}\Gamma^{-1}|1\rangle + \frac{\xi_{k_0} r}{2N} \langle 1|\Gamma\partial_{t_1}\hat{H}_o^{1D}\Gamma^{-1}|1\rangle}{N(E_{-1}-E_1)} \\ &= \frac{-\frac{\xi_{k_0}^* r}{2N} \frac{1}{2N} \left( \frac{\xi_{k_0}}{r} - \frac{r}{\xi_{k_0}} \right) - \frac{\xi_{k_0} r}{2N} \frac{1}{2N} \left( \frac{\xi_{k_0}}{r} - \frac{r}{\xi_{k_0}} \right)}{N(E_{-1}-E_1)} \\ &= \frac{r(\xi_{k_0} + \xi_{k_0}^*)}{4N^3(E_{-1}-E_1)} \left( \frac{r}{\xi_{k_0}} - \frac{\xi_{k_0}}{r} \right). \end{aligned} \quad (\text{S32})$$

The above term is non-zero when  $\xi_{k_0} + \xi_{k_0}^* \neq 0$  and  $\frac{r}{\xi_{k_0}} - \frac{\xi_{k_0}}{r} \neq 0$ , which is usually satisfied by the non-Hermitian case ( $r \neq 1$ ).

Eq. (S32) tends to be infinite when the system approximates to the phase boundary ( $(E_{-1}-E_1) \rightarrow 0$ ).

In conclusion, by analyzing the singularity of the values on  $\{C_{i,A}^\dagger|\text{Vac}\rangle\langle \text{Vac}|C_{i,B}|i \in [1, N]\}$ , we show that the gap closure point (phase transition point) where  $E_{\pm 1} = 0$  corresponds to the infinity of the  $\mathbb{L}_1$ -norm term in Gaussian kernel, which leads to the zero kernel value as well as the non-diffusion probability. In such sense, the choice of the raw data we have made here is reasonable and can be used for classifying the topological phases via the diffusion map method.

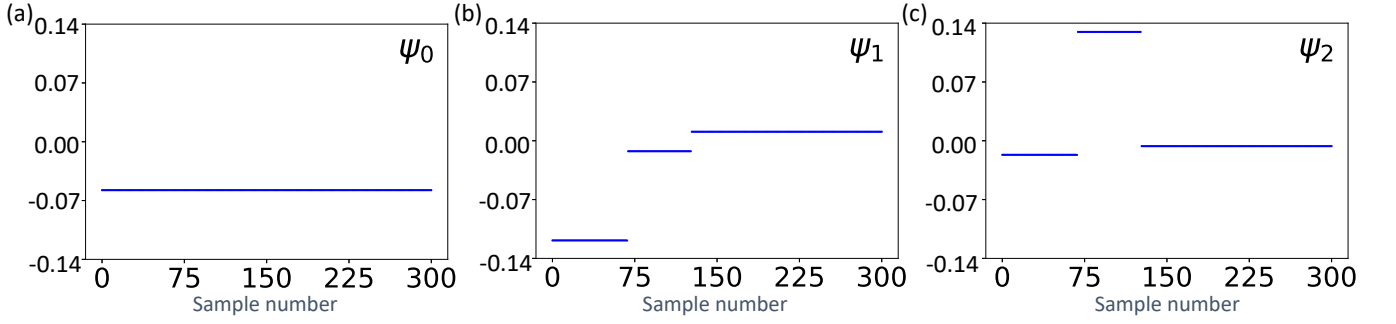


FIG. S1. 1D Non-Hermitian SSH model with PBC. Parameters: number of unit cells  $N = 160$ ,  $t_2 = 1$ , non-Hermitian term  $\gamma = 0.3$ ,  $t_1 \in [0, 3.0695]$ , samples interval  $\delta t_1 = 1/\pi^4$ ,  $\epsilon = 0.001$ . (a-c) Three right eigenvectors  $\psi_{0,1,2}$  with the corresponding eigenvalues  $\lambda_{0,1,2} \approx 1$ . The horizontal axis denotes the sample number, and the vertical axis denotes the coefficients of each sample site in eigenvectors. It is easy to verify that the two jumping points in the figures exactly match with the theoretically predicted phase transition points  $t_1 = 0.7$  and  $t_1 = 1.3$ . The three types of topological phases are clustered around the points  $(-0.0577, -0.1148, 0.0338)$  with 69 samples,  $(-0.0577, -0.0348, -0.1262)$  with 58 samples,  $(-0.0577, 0.0120, -0.0049)$  with 173 samples in  $\mathbb{R}^3$  respectively, which can be easily projected onto a 2D plane for visualization. The result matches the theoretically predicted phase transition points  $t_1 = 0.7$  and  $t_1 = 1.3$ .

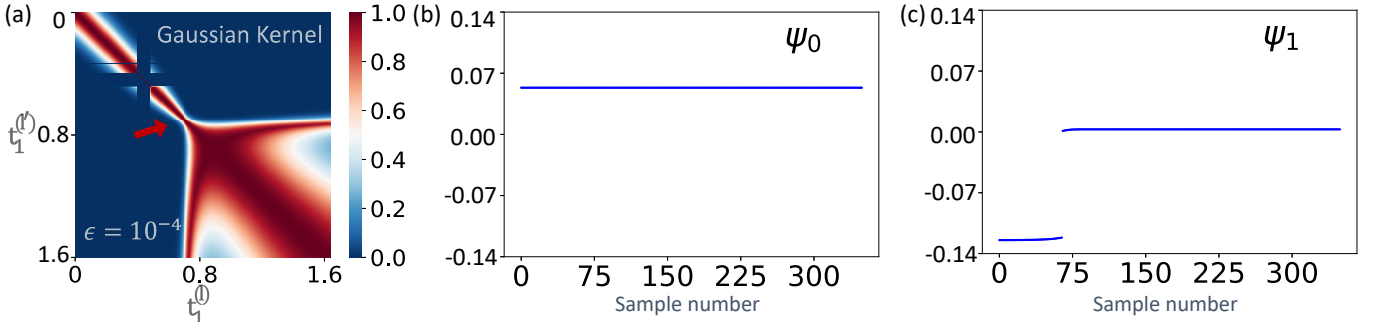


FIG. S2. 1D Non-Hermitian SSH model with OBC. Parameters: number of unit cells  $N = 40$ ,  $t_2 = 0.6$ , non-Hermitian term  $\gamma = 0.4$ , samples interval  $\delta t_1 = 1/\pi^5$ . (a) Heatmap for Gaussian kernel matrix of samples  $\mathbf{x}^{(l)}$  with varying  $t_1 \in [0, 1.6306]$ , hyper parameter  $\epsilon = 1 \times 10^{-4}$ . The non-diffusion zone around  $t_1 \approx 0.3921$  originates from the singularity of parameter  $r^{-1} = \sqrt{|(t_1 + \gamma)/(t_1 - \gamma)|} \rightarrow \infty$ . (b, c) Hyper parameter  $\epsilon = 1 \times 10^{-6}$ , for samples  $\{\mathbf{x}^{(l)}\}$  with  $t_1^{(l)}$  varying from 0.4902 to 1.6306, two right eigenvectors  $\psi_{0,1}$  of  $\mathcal{P}$  with the eigenvalues  $\lambda_{0,1} \approx 1$ , which indicate the two different topological phases in non-Hermitian SSH model in OBC. In (b, c), the horizontal axis denotes the sample number, and the vertical axis denotes the coefficients of each sample site in eigenvectors. Each sample  $\mathbf{x}^{(l)}$  with  $N = 80$  features can be mapped to the reduced two dimensional feature space  $((\psi_0)_i, (\psi_1)_i)$ . The 350 samples  $\{\mathbf{x}^{(l)}\}$  with varying  $t_1^{(l)} \in [0.4902, 1.6306]$  are clustered into two parts around the points  $(0.0535, -0.1223)$  with 65 samples and  $(0.0535, 0.0025)$  with 285 samples. The phase transition point can be directly observed from the eigenvectors.

### MORE DETAILED NUMERICAL RESULTS OF FIG. 2 AND FIG. 3 IN THE MAIN MANUSCRIPT

Here for details, we plot the eigenvectors of the one-step diffusion probability matrix  $\mathcal{P}$  with the corresponding eigenvalues  $\lambda_i \approx 1$ . We have the following four cases in total: the 1D non-Hermitian SSH and the 2D non-Hermitian QWZ models with PBC and OBC respectively, see Figs. (S1, S2, S3, S5).

### DIFFUSION MAP IN CLASSIFYING PHASES WITH GAPLESS BAND SPECTRA

In this work, we have studied the classification of the 2D NH QWZ model with PBC based on the diffusion map algorithm. Theoretically, for PBC the diffusion map cannot be directly utilized for clustering topological phases with the gapless bulk spectra, since the input data  $\hat{d}(k) = \frac{\vec{d}}{\sqrt{\vec{d}^2}}$  could be singular at the gapless momentum points. The reason has been shown in Sec. , which demonstrates that the samples with the gapless point  $(\vec{d})^2 = 0$  lead to the zero diffusion probability, and the kernel matrix is separated into diagonal blocks by such samples. Adding samples at exactly or near the gapless point could result in artificial zero diffusion probability, and consequently lead to more predicted phases than the true number of phases hosted by

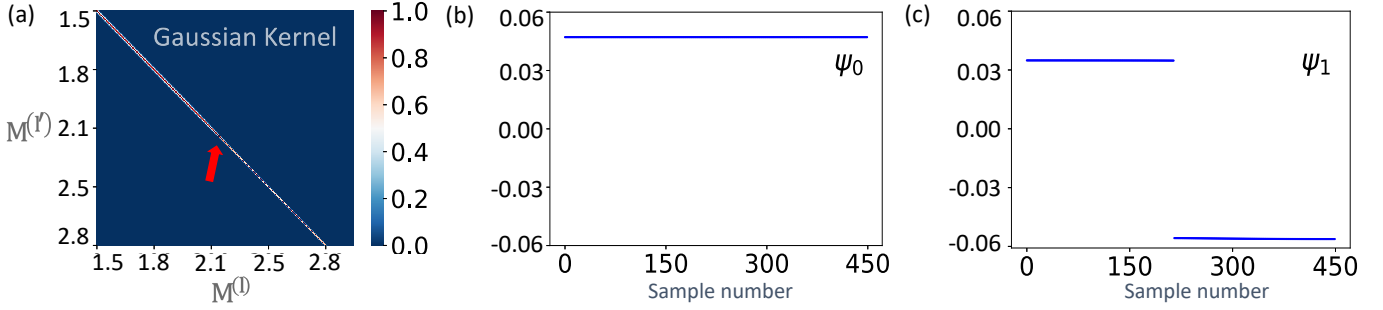


FIG. S3. 2D non-Hermitian QWZ model with OBC. Parameters: number of unit cells  $N = 24 \times 24 = 576$ ,  $t_x = t_y = 1$ ,  $v_x = v_y = 1$ , non-Hermitian term  $\gamma_x = \gamma_y = \sqrt{5}/5$ , samples interval  $\delta M = 1/\pi^5$ ,  $M \in [1.4705, 2.9377]$ ,  $\epsilon = 5 \times 10^{-9}$ . (a) Heatmap of the Gaussian kernel values. The red arrow indicates the phase transition point. (b, c) Two right eigenvectors  $\psi_{0,1}$  of  $\mathcal{P}$  with the eigenvalues  $\lambda_{0,1} \approx 1$ , which indicate the two different topological phases in non-Hermitian QWZ model in OBC. In (b, c), the horizontal axis denotes the sample number, and the vertical axis denotes the coefficients of each sample site in eigenvectors. Each sample  $\mathbf{x}^{(l)}$  with  $N = 576$  features can be mapped to the reduced two dimensional feature space  $((\psi_0)_l, (\psi_1)_l)$ . With such two eigenvectors, the 450 samples  $\{\mathbf{x}^{(l)}\}$  with varying  $M$  are clustered into two parts around two points:  $(0.0471, 0.0348)$  with 215 samples and  $(0.0471, -0.0560)$  with 235 samples. Each part corresponds to one topological phase.

the system.

We first introduce how to identify the artificial phase boundaries owing to the samples with the gapless spectra. Given the parameter region of a Bloch Hamiltonian, one can obtain different sample sets by choosing different lattice sizes. Although different lattice size leads to the different feature dimension of an input sample, the matrix dimensions of kernels for different lattice sizes are the same due to that the number of samples in each set are the same. The mechanism for detection is simple: If the gapless bulk spectrums only occur at the phase boundaries (usually with the gapless spectra at the momentum 0 or  $\pi$ ), then the block boundaries of the kernel matrices should be same for different lattice sizes, hence the diffusion map approach applies directly. While there exist phases with gapless spectra, like the 2D NH QWZ model, the appearance of momenta for the gapless bulk spectra would depend on the choice of lattice sizes (note that for different lattice sizes, the discrete momentum points are different after the Fourier transformation), i.e., whether the momenta for gapless bulk spectra is in the discrete momentum set. Hence the blocks of the corresponding kernel matrices may change with the varying lattice sizes, then the failure of the machine learning method can be detected by directly comparing the classification results in different lattice sizes. At the phase transition point, the gapless momentum  $k_0$  is usually 0 or  $\pi$ , whose appearance in discrete momentum configuration is independent of the lattice sizes. Those invariant block boundaries with varying lattice sizes are the real phase boundaries. We take the 2D NH QWZ model as an example, detailed numerical calculations in Fig. S4 show that the artificial phases boundaries appear owing to the samples with the gapless momenta within the gapless phases region.

To circumvent the above obstacle, one can construct an “effective” Gaussian kernel matrix by simply averaging the kernel matrices of different input sample sets with varying lattice sizes (different discrete momentum configurations), so that the artificial zero diffusion probabilities become nonzero after the average. The example of the 2D NH QWZ model is shown in Fig.S5.

## DISCREPANCY OF THE DIFFUSION MAP ALGORITHM IN PREDICTING PHASE BOUNDARIES

In locating the phase boundaries of models with PBC, the diffusion map algorithm performs high accuracy, i.e., the discrepancy between the learned phase boundaries and the theoretical ones is very small. In the case of OBC, the phase boundaries predicted by the unsupervised method behave  $\sim 1\%$  discrepancy. We conclude that the following reasons lead to the discrepancy.

- 1) One prominent reason for the discrepancy should be the finite size of the model we study here. The numerical calculated phase boundary approximates to the theoretical one when the size tends to be infinite. We carry out numerical calculations to support this point. For the 1D NH SSH model with OBC, we numerically obtain the input data with different model sizes for the diffusion map algorithm. We choose the same parameters as in the main manuscript with the theoretical phase transition point 0.7211. We obtain that when the number of unit cells  $N=60$ , the learned phase transition point is 0.6862; When  $N=80$ , the learned phase transition point is 0.6993; When  $N=100$ , the learned phase transition point is 0.7058. Fig. S6 demonstrates that with the model size increasing, the discrepancy between the learned phase transition point and the theoretical prediction tends to be smaller.

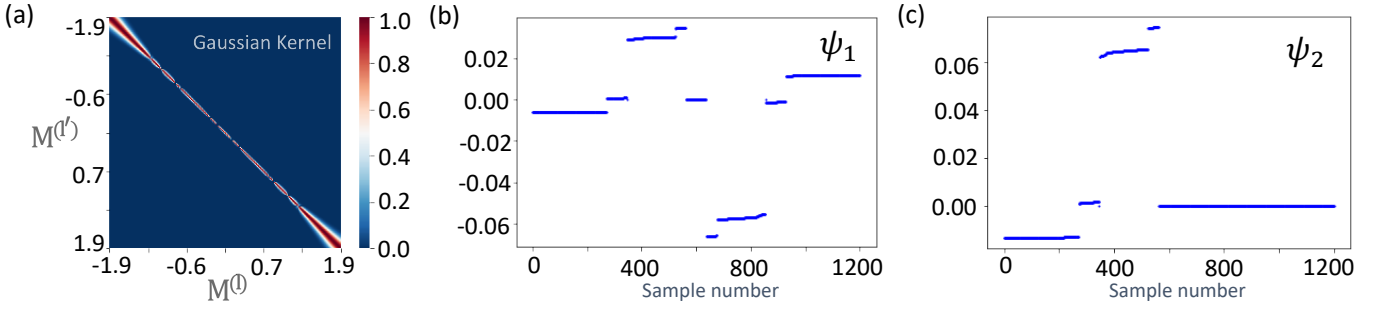


FIG. S4. 2D non-Hermitian QWZ model with PBC. Failed classification of samples with gapless momenta in the gapless regions of Hamiltonian. Parameters: number of unit cells  $N = 20 \times 20 = 400$ ,  $t_x = t_y = 0.5$ ,  $v_x = v_y = 0.5$ , non-Hermitian terms  $\gamma_x = 1/\sqrt{32}$ ,  $\gamma_y = 1/\sqrt{32}$ ,  $\gamma_z = 0$ .  $M \in [-1.9607, 1.9574]$  with the interval  $\delta t_1 = 1/\pi^5$ , number of samples: 1200, hyper parameter  $\epsilon = 0.001$ . The six theoretical phase boundaries should be  $\{\pm 1.25, \pm 0.75, \pm 0.25\}$ . (a) Heatmap of the Gaussian kernel values. It is obvious that there are more than seven blocks, which is beyond the theoretical predicted clusters of phases. This is due to the existence of gapless momenta in discrete momentum configuration within the gapless phase regions. (b-c) Two eigenvectors  $\psi_{1,2}$  of diffusion matrix  $\mathcal{P}$  with eigenvalues  $\lambda_{1,2} \approx 1$ . From the diagrams of eigenvectors, one observes that the samples are clustered into at least nine parts labeled by different  $M$  domains:  $[-1.9607, -1.0751]$ ,  $[-1.0718, -0.8300]$ ,  $[-0.8267, -0.2516]$ ,  $[-0.2484, -0.1209]$ ,  $[-0.1176, 0.1209]$ ,  $[0.1242, 0.2484]$ ,  $[0.2516, 0.8300]$ ,  $[0.8333, 1.0718]$ ,  $[1.0751, 1.9574]$ . Owing to the accuracy of the figures, one can not directly observe the real phase boundaries  $\pm 1.25$  and  $\pm 0.75$  from the figures. Such phase boundaries can be located by checking the numerical data of the two eigenvectors  $\psi_{1,2}$ . The artificial phase boundaries originate from the samples with the gapless momenta in the gapless phase regions.

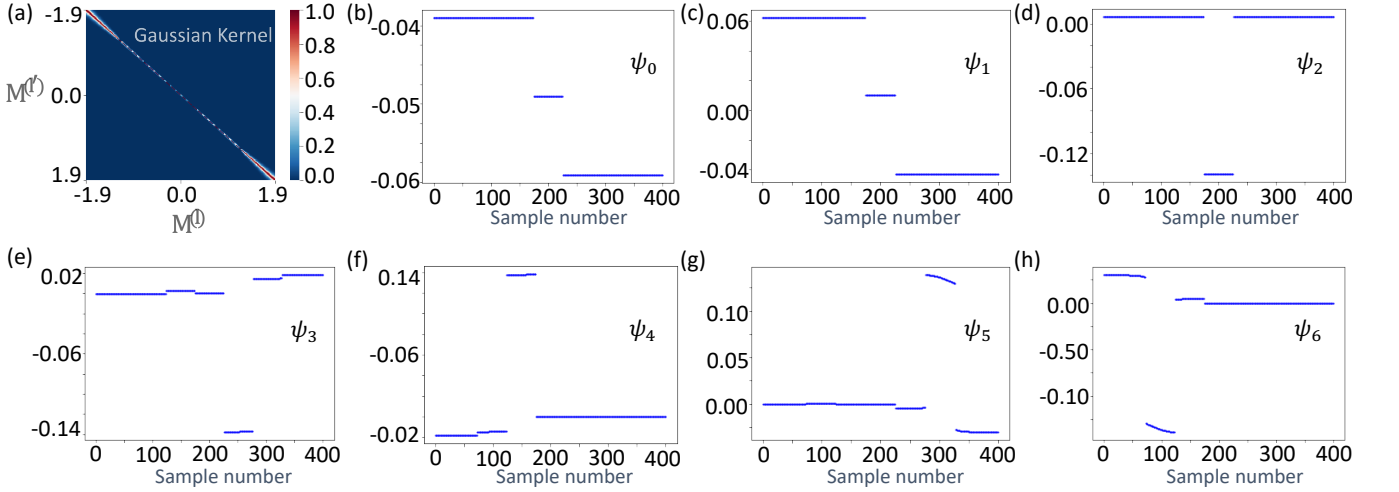


FIG. S5. 2D non-Hermitian QWZ model with PBC. Successful classification of samples with gapless momenta in the gapless regions of Hamiltonian. Parameters: number of unit cells  $N = 20 \times 20 = 400$ ,  $t_x = t_y = 0.5$ ,  $v_x = v_y = 0.5$ , non-Hermitian terms  $\gamma_x = 1/\sqrt{32}$ ,  $\gamma_y = 1/\sqrt{32}$ ,  $\gamma_z = 0$ .  $M \in [-1.9607, 1.9509]$  with the interval  $\delta t_1 = 3/\pi^5$ , number of samples: 400, hyper parameter  $\epsilon = 0.00005$ . (a) Heatmap of the “effective” Gaussian kernel matrix, as an average of a set of seven kernel matrices with varying number of unit cells  $N = \{14 \times 14, 16 \times 16, 18 \times 18, 20 \times 20, 22 \times 22, 24 \times 24, 26 \times 26\}$ . (b-h) Seven eigenvectors  $\psi_{0 \sim 6}$  of diffusion matrix  $\mathcal{P}$  with the largest seven eigenvalues  $\lambda_{0 \sim 6} \approx 1$ . From the diagrams of eigenvectors, one obtains that the samples are clustered into seven parts labeled by different  $M$  domains:  $[-1.9607, -1.2548]$ ,  $[-1.2450, -0.7549]$ ,  $[-0.7451, -0.2549]$ ,  $[-0.2451, 0.2451]$ ,  $[0.2549, 0.7451]$ ,  $[0.7549, 1.2450]$ ,  $[1.2548, 1.9509]$ . In comparison with Fig. S4, the artificial phase boundaries here are eliminated by averaging the kernel matrices with different lattice sizes.

- 2) Another reason should be that we choose only part of the projective matrix as the input raw data. For example, in the 1D NH SSH model with  $N$  unit cells, to circumvent the obstacle of NHSE, we just choose a small part, i.e.,  $N$  out of  $4N^2$  projective matrix elements for each sample as the input data. This can be regarded as a trade-off between the compression of features and the training precision. The similar trade-off also exists in another work [92] of the CNN-based supervised learning topological phases based on the experimental data. In that work, the authors showed that the trained CNN could successfully identify (with a probability  $> 90\%$ ) different topological phases with less than 10% of the experimental data.
- 3) In addition, for the 2D NH QWZ model with OBC, the theoretical predicted phase boundary itself is an approximation, which is based on the perturbation theory. In the original paper of the 2D NH QWZ model [42], there already exists discrepancy ( $\sim 0.6\%$  for  $M \approx 2.2$ ) between the theoretical phase transition point and the numerical results. This also



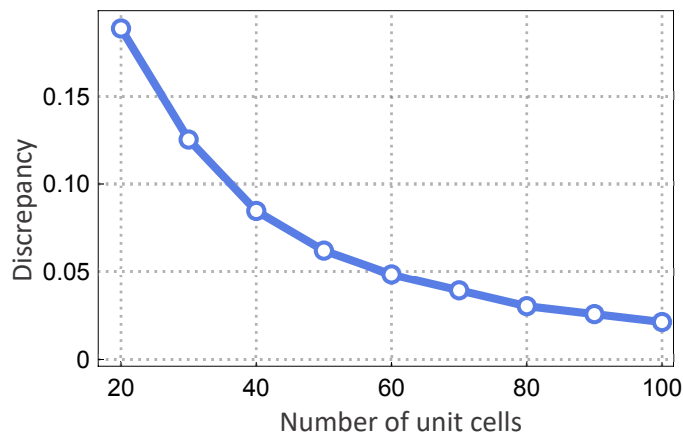


FIG. S6. Discrepancy between the learned phase transition point and the theoretical prediction of the 1D NH SSH model with OBC. The discrepancy tends to be smaller with the number of unit cells increasing.

contributes to the discrepancy which appears in our learned results.

#### UNSUPERVISED LEARNING OF 2D NH QWZ MODEL WITH PBC BY VARYING OTHER PARAMETERS

In the main manuscript, we successfully classify the non-Hermitian topological phases in an unsupervised fashion. For the 2D NH QWZ model with PBC, the samples are obtained by varying the parameter  $M$ . Here for completeness, we utilize the diffusion map to classify samples generated by varying other parameters. To circumvent the obstacle posed by the samples with the gapless momenta within the gapless regions, here we choose the “effective” kernel matrix mentioned in Sec. for the diffusion map algorithm.

Firstly, we discuss the case of varying the parameter  $t_x$  while fixing other parameters. Without loss of generality, one can set  $v_x = v_y = 1$ ,  $\gamma_x = 0.6$ ,  $\gamma_y = 0.8$ ,  $\gamma_z = 0$ ,  $M = 2$  and  $t_y = 2$ . Then from Eq. S13 one can theoretically obtain seven phases, with the theoretical phase boundaries  $t_x = \{-5, -3, -1, 1, 3, 5\}$ . Detailed numerical calculations based on the diffusion map method show that the seven different phases are successfully classified, see Fig. S7 for details.

Then we discuss the case of varying the parameter  $\gamma_x$  and keeping other values fixed. Numerical results show that the phases are successfully classified, see Fig. S8 for details.

#### DISCUSSION ABOUT THE OBSTACLE POSED BY NHSE IN MACHINE LEARNING METHODS

In this section, we would like to make a discussion about the universality of obstacle owing to NHSE for different machine learning methods. Recently, a number of unsupervised learning methods have been proposed to classify topological phases, such as clustering, variational autoencoders, divergence-based predictive method, learning by confusion, topological data augmentation, and so on [93–104]. However, most of these methods are based on convolutional neural network (CNN) and have only been applied to Hermitian systems. For non-Hermitian systems with NHSE, since all the eigenstates are exponentially localized at the boundaries, the relevant features could be dramatically suppressed and consequently are hard to extract. This leads to a notable obstacle owing to the NHSE, independent of which learning algorithm is utilized. In a recent work [91], the authors successfully predicted the topological phases of non-Hermitian SSH model in the momentum space with PBC based on the supervised CNN machine learning method. However, they noted that the CNN algorithm for learning the non-Hermitian models in the momentum space (with PBC) could not carry over to the non-Hermitian topological phases with the skin effect in the real space (with OBC), and further studies on NHSE and the classification of non-Hermitian topological phases with OBCs based on machine learning algorithms would be conducted. The unsupervised methods based on CNN would suffer the same obstacle owing to NHSE as for the diffusion map method.

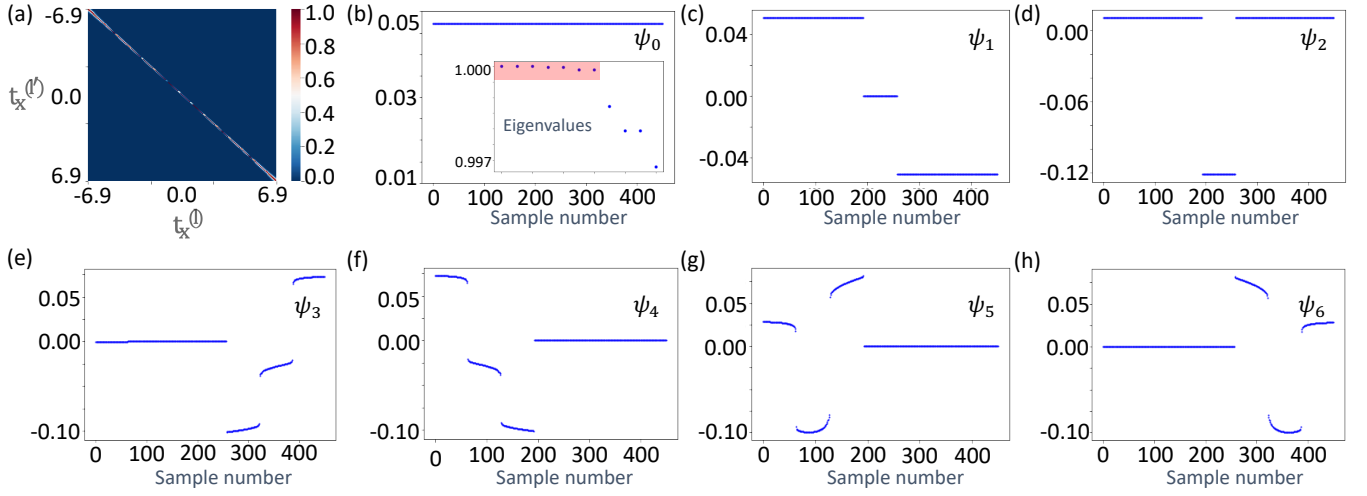


FIG. S7. 2D non-Hermitian QWZ model with PBC, samples are generated by varying parameter  $t_x$ . Parameters:  $v_x = v_y = 1$ ,  $\gamma_x = 0.6$ ,  $\gamma_y = 0.8$ ,  $\gamma_z = 0$ ,  $M = 2$  and  $t_y = 2$ .  $t_x \in [-6.9295, 6.9295]$  with the interval  $\delta t_1 = 3/\pi^4$ , number of samples: 450, hyper parameter  $\epsilon = 0.00015$ . (a) Heatmap of the "effective" Gaussian kernel matrix, as an average of a set of five kernel matrices with varying number of unit cells  $N = \{18 \times 18, 20 \times 20, 22 \times 22, 24 \times 24, 26 \times 26\}$ . (b-h) Seven eigenvectors  $\psi_{0 \sim 6}$  of the  $\mathcal{P}$ -matrix with the largest eigenvalues  $\lambda_{0 \sim 6} \approx 1$ . (b) also contains the figure of seven largest eigenvalues (red area) of the "effective" diffusion matrix  $\mathcal{P}$ . From the diagrams of eigenvalues and eigenvectors, one obtains that the samples are clustered into seven parts labeled by different  $t_x$  domains:  $[-6.9295, -5.0201]$ ,  $[-4.9893, -3.0182]$ ,  $[-2.9874, -1.0163]$ ,  $[-0.9855, 0.9855]$ ,  $[1.0163, 2.9874]$ ,  $[3.0182, 4.9893]$ ,  $[5.0201, 6.9295]$ . The numerical calculated phase boundaries coincide with the theoretical ones  $t_x = \{-5, -3, -1, 1, 3, 5\}$  with a low discrepancy.

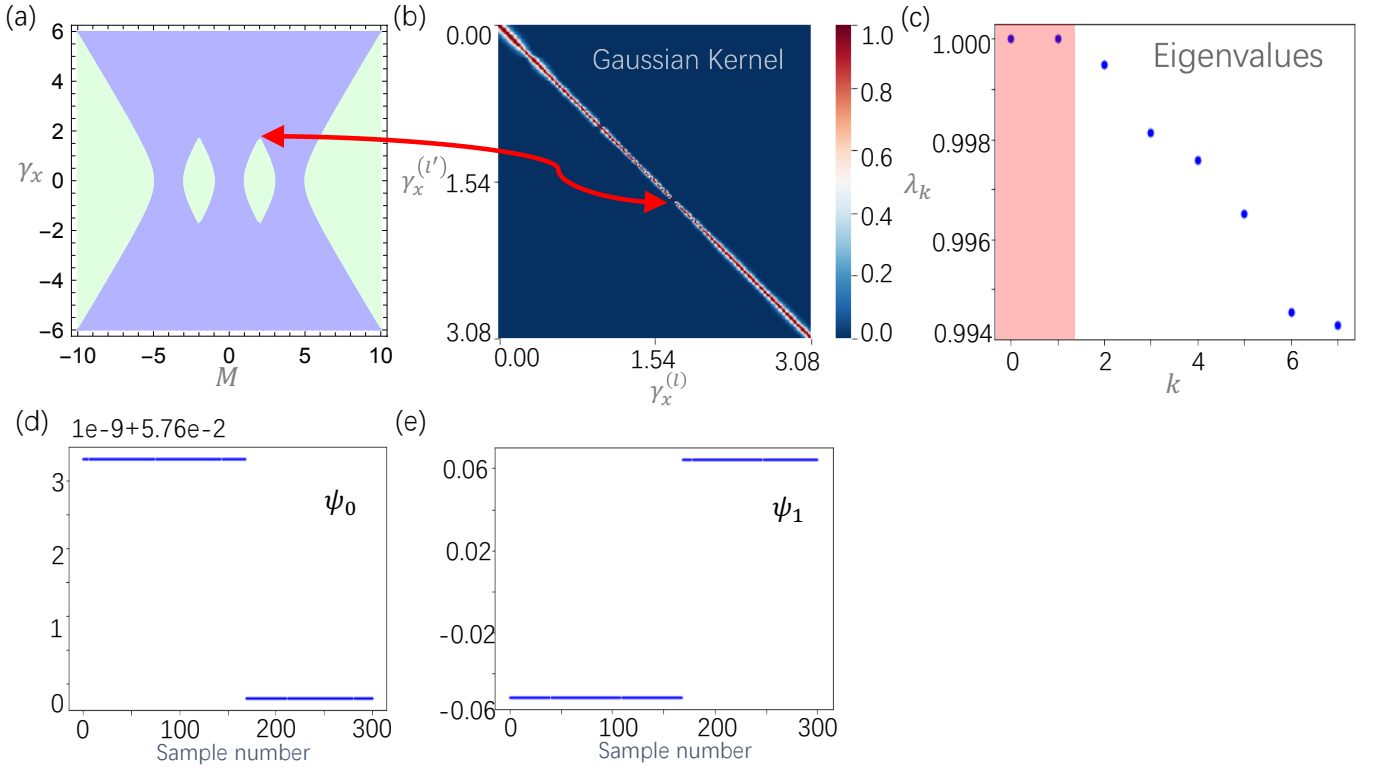


FIG. S8. 2D non-Hermitian QWZ model with PBC, samples are generated by varying parameter  $\gamma_x$ . Parameters:  $t_x = t_y = 2$ ,  $v_x = v_y = 0.5$ , non-Hermitian terms  $\gamma_y = 1$ ,  $\gamma_z = 0$ ,  $M = 2$ .  $\gamma_x \in [0, 3.0798]$  with the interval  $\delta t_1 = 1/\pi^4$ , number of samples: 300, hyper parameter  $\epsilon = 0.001$ . (a) Theoretical phase diagram of 2D NH QWZ model with PBC, parameters  $t_x = t_y = 2$ ,  $v_x = v_y = 0.5$ ,  $\gamma_y = 1$ ,  $\gamma_z = 0$ . The horizontal axis represents the value of parameter  $M$ , and the vertical axis represents the value of parameter  $\gamma_x$ . The green area represents the gapped phases with well defined topological indices, whereas the purple area represents the gapless phase without well defined topological indices. In the parameter region  $\{M = 2, \gamma_x \in [0, 3.0798]\}$ , there is only one phase boundary at  $\gamma_x = \sqrt{3} \approx 1.7321$ . (b) Heatmap of the “effective” Gaussian kernel matrix, as an average of a set of six kernel matrices with varying number of unit cells  $N = \{20 \times 20, 22 \times 22, 24 \times 24, 26 \times 26, 28 \times 28, 30 \times 30\}$ . The red arrow line connects the corresponding phase boundary between the theoretical (a) and numerical results (b). (c) The largest eigenvalues of “effective” diffusion matrix  $\mathcal{P}$ . (d-e) Two eigenvectors  $\psi_{0,1}$  of  $P$ -matrix with the largest eigenvalues  $\lambda_{0,1} \approx 1$ . From the diagrams of eigenvectors, the samples are clustered into two parts labeled by different  $\gamma_x$  domains: phase with the gapped spectra  $[0, 1.7350]$  and phase with the gapless spectra  $[1.7452, 3.0798]$ . The numerical calculated phase boundary  $\gamma_x \approx 1.7350$  coincides with the theoretical one  $\gamma_x \approx 1.7321$  with a low discrepancy.